

**DIMENSION DEPENDENT OPTOELECTRONIC
PROPERTIES OF CESIUM LEAD HALIDE
PEROVSKITES**

**A Thesis Submitted to
the Graduate School of Engineering and Sciences of
İzmir Institute of Technology
in Partial Fulfillment of the Requirements for the Degree of**

MASTER OF SCIENCE

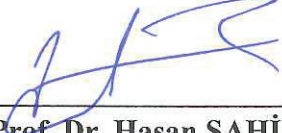
in Photonics Science and Engineering

**by
Mehmet ÖZCAN**

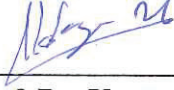
**June 2019
İZMİR**

We approve the thesis of Mehmet ÖZCAN

Examining Committee Members:



Assoc. Prof. Dr. Hasan ŞAHİN
Department of Photonics, İzmir Institute of Technology



Assoc. Prof. Dr. Yaşar AKDOĞAN
Department of Material Science and Engineering, İzmir Institute of Technology

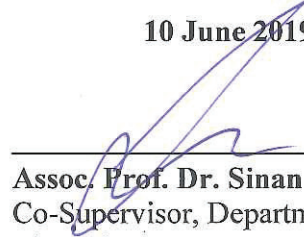


Assoc. Prof. Dr. Engin DURGUN
Department of Materials Science and Nanotechnology, Bilkent University

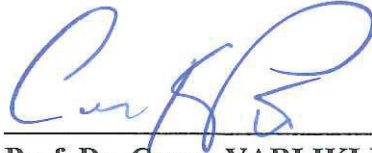
10 June 2019



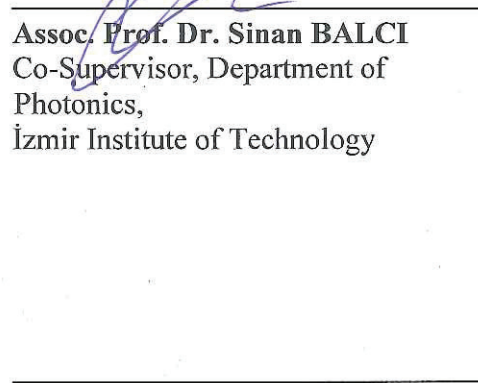
Assoc. Prof. Dr. Hasan ŞAHİN
Supervisor, Department of Photonics,
İzmir Institute of Technology



Assoc. Prof. Dr. Sinan BALCI
Co-Supervisor, Department of
Photonics,
İzmir Institute of Technology



Prof. Dr. Canan VARLIKLI
Head of the Department of Photonics



Prof. Dr. Aysun SOFUOĞLU
Dean of Graduate School of
Engineering and Science

ACKNOWLEDGMENTS

First of all, I would like to thank my supervisor Assoc. Prof. Dr. Hasan Şahin for his patient instruction, generous help and support in my master study and this thesis work.

I acknowledge, my co-supervisor Assoc. Prof. Dr. Sinan Balcı for his unconditional support and help.

I would like to acknowledge and thank the committee members of my thesis Assoc. Prof. Dr. Yaşar Akdoğan and Assoc. Prof. Dr. Engin Durgun for their participation.

I would also like to thank Prof. Dr. Mustafa M. Demir, Gökhan Topçu, Tuğrul Güner, Yenal Yalçınkaya, Meriç Güvenç, Alper Yanılmaz and Aysel Tomak for Raman, PL, XRD, UV-VIS absorption spectrum measurements and perovskite synthesis.

I would like to give my dearest thank my colleagues Barış Akbalı, Zeynep Kahraman, Elif Ünsal, Fadıl İyikanat, Ali Kandemir, Sercan Özen, Efsun Tekneci and my best friends Yağız Oyun, Anıl Kolay, Utku Canpolat, Sevgi Serkir, Hatice İlhan, Gülçin Dönmez for their unique friendship and special motivation at difficult times.

Most importantly, I would like to thank my family and my love Helin Yıldırım for everything they have done.

Finally, a special mention goes to my late lecturer and friend, Dr. H. Duygu Özaydın who always believed in me and supported me. I would never have been able to come to this point without her nice advices about the life. I dedicated this thesis to her.

This research was supported by TUBITAK with 117F095 project number.

ABSTRACT

DIMENSION DEPENDENT OPTOELECTRONIC PROPERTIES OF CESIUM LEAD HALIDE PEROVSKITES

All-inorganic cesium lead halide perovskites (ILHPs), are gaining wide variety of role as strong contenders due to their extraordinary photovoltaic features in optoelectronic research with tunable band-gap, large absorption cross-section, long carrier lifetime, and high carrier mobility. Most of the initial studies focused on bulk-like perovskite materials, while the rapidly growing colloidal perovskite nanocrystals impress additional interest because of their unique properties. In this thesis, colloidal lead halide perovskite nanocrystals' optoelectronic properties are investigated and associated with their size and dimensionality.

The photoluminescence characteristics of colloidal lead halide perovskite nanocrystals can be tuned by reducing their dimensionality. Thin layer fabrication of CsPbBr₃ films which consist of 2D lead halide perovskite nanoplatelets, is achieved by a novel coating approach via electrospraying from precursor solution. Electrospraying method represents not only a new and fast perovskite film fabrication but also dimensional tunability by changing the amount of oleylamine which is intercalating agent. Moreover, thickness-dependence of the structural, electronic and vibrational properties of orthorhombic CsPbI₃, which is one of the most stable phase at room temperature, is investigated by means of state-of-the-art first-principles calculations. It is also investigated that the electronic band gap increases with decrease in perovskite thickness due to quantum size effect. Lastly, it is investigated that water induced transition to form large bundles of CsPbBr₃ nanowires show a redshifted photoluminescence. Water molecule causes the detachment of ligands from the perovskite surface which leads to form bundles.

In summary, this thesis provides an understanding of dimension dependent optoelectronic properties of lead halide perovskite.

ÖZET

SEZYUM KURŞUN HALOJENÜR PEROVSKİTLERİN BOYUTA BAĞLI OPTOELEKTRONİK ÖZELLİKLERİ

Tamamen inorganik sezyum kurşun halojenür perovskitleri (ILHP'ler), ayarlanabilir bant aralığı, uzun yük taşıyıcı ömrü gibi fotovoltaik özellikleri nedeniyle optoelektronik araştırmalarda güçlü bir rakip olarak geniş bir rol oynamaktadır. Daha önceki çalışmaların çoğu büyük boyutlu perovskit malzemeler üzerine odaklanırken, hızla çeşitliliği artan küçük boyutlu koloidal perovskit nanokristalleri benzersiz özellikleri nedeniyle ilgi çekmeye başlamıştır. Bu tezde küçük boyutlu koloidal kurşun halojenür perovskit nanokristallerin büyüklüğüne ve boyutuna bağlı olarak optoelektronik özellikleri araştırılmış.

Koloidal kurşun halojenür perovskite nanokristallerin fotoluminesans özellikleri, boyutlarının azaltılmasıyla ayarlanabilmektedir. Yeni ve kolay elektrosprey sistemi ile 2 boyutlu kurşun halojenür perovskit nano levhalardan oluşan CsPbBr_3 ince tabaka filmler elde edilmiştir. Elektrospreyleme yöntemi sadece yeni ve hızlı bir perovskit film imalatını değil aynı zamanda oyleamin miktarını değiştirerek boyutsal kontrolü de sağlamaktadır. Ayrıca, oda sıcaklığındaki en kararlı fazlardan biri olan ortorombik CsPbI_3 'ün yapısal, elektronik ve titreşim özelliklerinin kalınlığa bağımlılığı, DFT hesaplamaları ile incelenmiştir ve elektronik bant boşluğunun, perovskite kalınlığında, kuantum büyüklüğü etkisinden dolayı azalma ile arttığı da görülmüştür. Son olarak, suyun neden olduğu CsPbBr_3 nanotellerinin demetler halini alması ve PL spectrumda kırmızı yönünde kayma gösterdiği incelenmiştir. Bu kaymanın sebebinin, su molekülü perovskit nanotellerin yüzeyine tutunmuş ligantları kopararak, yüzeyleri boş kalan nanotellerin demetler oluşturmasından kaynaklandığı gözlenmiştir.

Sonuç olarak, bu tez, kurşun halojenür perovskitlerin boyuta bağlı optoelektronik özelliklerinin anlaşılmasını sağlamaktadır.

To dear Dr. H. Duygu Özaydın...

TABLE OF CONTENTS

LIST OF FIGURES	ix
CHAPTER 1. INTRODUCTION	1
CHAPTER 2. METHODOLOGY	5
2.1. Experimental Methodology	5
2.1.1. Cesium Lead Halide Perovskite Synthesis	5
2.1.1.1. Hot-Injection Method	5
2.1.1.2. Electrospraying Method	5
2.1.2. Characterization Techniques	6
2.1.2.1. UV-Vis Absorption Spectroscopy	6
2.1.2.2. Photoluminescence	7
2.1.2.3. Raman Spectroscopy	8
2.2. Computational Methodology	11
2.2.1. Density Functional Theory	11
2.2.1.1. Basics of Density Functional Theory	12
2.2.1.2. Hohenberg-Kohn Theorems	13
2.2.1.3. Hellmann-Feynman Theorem	13
2.2.1.4. The Kohn-Sham Equations	14
2.2.1.5. Functionals of Exchange and Correlation	15
2.3. Vasp Input Set	16
CHAPTER 3. COLOR TUNABLE ALL-INORGANIC PEROVSKITES SYNTHESIZED BY ELECTROSPRAYING	17
3.1. Thickness Tunable Nanoplatelet Growth	20
3.2. PL Evolution of Perovskite Nanoplatelet	22
3.3. Effect of Electrospray Conditions	24
3.4. Lithography Performance of Electrospraying Method	26

CHAPTER 4. ORTHORHOMBIC CsPbI ₃ PEROVSKITES: THICKNESS-DEPENDENT STRUCTURAL, OPTICAL AND VIBRATIONAL PROPERTIES	27
4.1. Possible Structures of Ultra-thin Orthorhombic CsPbI ₃	28
4.2. Electronic and Optical Properties of Ultra-thin CsPbI ₃	31
4.3. Enhanced Stability via Encapsulation	33
 CHAPTER 5. WATER-INDUCED DIMENSIONAL TRANSITION FROM CsPbBr ₃ NANOWIRE TO BUNDLES	 35
5.1. Water-induced Evolution from Blue to Green Light Emitting Structure	 36
 CHAPTER 6. CONCLUSIONS	 40
 REFERENCES	 42

LIST OF FIGURES

<u>Figure</u>	<u>Page</u>
Figure 2.1. Absorption and emission of photon schematic.	7
Figure 2.2. Optic Measurement setup in the Cent Lab.	9
Figure 2.3. Quantum energy transitions for Rayleigh and Raman scattering.	10
Figure 2.4. Horiba Xplora Plus Raman system in the Cent Lab.	11
Figure 3.1. Photographic image of electrospraying setup.	19
Figure 3.2. (a) Photographic image under daylight and under 254 nm UV light, (b) photoluminescence and (c) absorption spectra of perovskite films according to the amount of OAm in the presence of oleic acid (500 μ L). .	21
Figure 3.3. XRD diffractograms of (a) bare ITO substrate, (b) non-emissive, (c) green emitting, (d) cyan emitting, and (e) blue emitting perovskite films on ITO.	22
Figure 3.4. STEM images of (a) green emitting and (b) blue emitting perovskite films.	23
Figure 3.5. Time dependent PL evolution of blue emitting perovskite film under UV light.	24
Figure 3.6. PL spectra of control sample with different (a) flow rate, (b) applied potential, and (c) reagent concentration.	25
Figure 3.7. Patterned perovskite film on ITO, under daylight and UV light (254 nm).	26
Figure 4.1. (a) Bulk, (b) bilayer, (c) monolayer structures of CsPbI ₃ crystal.	29
Figure 4.2. Phonon band diagram of (a) bulk CsPbI ₃ crystal in orthorhombic phase, (b) Cs ₃ Pb ₂ I ₇ and Cs ₂ Pb ₃ I ₈ bilayers, (c) Cs ₂ PbI ₅ , CsPbI ₄ , and Cs ₂ PbI ₄ monolayers.	29
Figure 4.3. Electronic band dispersions of (a) bulk, (b) bilayer, (c) monolayer structures of orthorhombic CsPbI ₃ crystal. The layer dependent opti- cal properties of CsPbI ₃ . (a) Imaginary part of dielectric function, (b) absorption coefficient, (c) reflectivity, and (d) transmissivity of bulk, bilayer, and monolayer CsPbI ₃	32

Figure 4.4. Molecular dynamics simulations of Cs ₂ PbI ₄ monolayer (a) at 300 K for 5 ps, (b) from 0 to 500 K for 2 ps, (c) from 0 to 500 K for 5 ps.	34
Figure 5.1. Images of CsPbBr ₃ ; (a) at first after drop-casting, (b) 24 hours and (c) 144 hours after water treatment, respectively under daylight and UV light. The focused area in (d) shows an optic microscope images under daylight and UV light.	36
Figure 5.2. (a) Time-dependent photoluminescence of NWs interacting with water, (b) SEM image after 24 hours of interaction with the resulting NW structure, and (c)-(d) are both as-synthesized and water-interacted samples' XRD measurement and Raman spectra. Scale bars are 2 μm.	37
Figure 5.3. (a) Cs-terminated and (b) Pb-terminated surfaces of CsPbBr ₃	38

CHAPTER 1

INTRODUCTION

Modern life develops around the energy and technological advances and all new inventions increase the energy demand. Our style of living relies on energy which even essential services are impossible without a energy source. On the other hand, the consequences of our energy misuse can no longer be tolerated by the planet, the accumulation of indifferent energy usage over the last 200 years has caused a huge climate crisis on Earth. Especially for some species, extinction seems unavoidable.

The way we produce energy is one of the strong causes of climate change. That is why the best solution is renewable energy sources in order to overcome this issue for now and the future. The implementation of renewable energy can be a starting point for acting towards the heart of this issue. The key parameter for this revolution is that the solution needs to be seemed cost reduction. Especially for renewable energy, low-cost material research has high priority.

Perovskites are promising material for the future in this regard. The perovskite research has just started, but despite marketing issues, the overall results are already attracting energy players.

In 1839 Gustav Rose discovered CaTiO_3 and the mineral was named after Russian mineralogist Lev Perovski.(Rose, 1839) Since then, perovskite is named as ABX_3 , the identical crystal structure as CaTiO_3 . It was not known as a fascinating semiconductor until scientists concentrated on a specific type of organic hybrid perovskite at the beginning of the 1990s.(Mitzi *et al.*, 1995; Liang *et al.*, 1998; Hong *et al.*, 1992b; Kagan *et al.*, 1999)

Perovskite material has an ABX_3 general formula. A is organic such as CH_3NH_3^+ (MA), $\text{HC}(\text{NH}_2)_2^+$ (FA) or inorganic such as Cs^+ cation, B is metal cation as Pb^{2+} , Sn^{2+} , Sb^{2+} , and X is halide anion as Br^- , Cl^- , I^- in the crystal structure. The first type and second type are known as organic-inorganic perovskite and the all-inorganic perovskite, respectively. The discovery of MAPbI_3 as a photosensitizer in solar cell (DSSC's) in 2009 has led to more attention being paid to these materials.(Kojima *et al.*, 2009)

Among those, all-inorganic cesium lead halide perovskites (ILHPs) have attracted tremendous attention for recent years. Due to their extraordinary photovoltaic features, ILHPs are gaining wide variety of role as strong contenders in optoelectronic research with tunable band-gap, large absorption cross-section, long carrier lifetime, and high carrier mobility.(Protesescu *et al.*, 2015; Akkerman *et al.*, 2015; Makarov *et al.*, 2016; Stranks *et al.*, 2013) Therefore, the fabrication of ILHP nanostructures with controllable composition, morphology, dimensionality, and orientation have become important as a first step, in order to employ the superior properties in photovoltaics.

Since their applicability in photovoltaics including solar cells and light-emitting diodes (LEDs) the fabrication methods of perovskite thin films with desired shape and size is crucial. For instance, the large crystal size or grain boundaries decrease the electroluminescence (EL) performance of perovskite light-emitting diodes (PeLEDs) because of trap states.(Cho *et al.*, 2017; Wei *et al.*, 2016; Pan *et al.*, 2016) The probability for non-radiative recombination in large-sized crystals mostly increases, which results in a low EL efficiency for PeLEDs.(Kim *et al.*, 2016; Cho *et al.*, 2015) Similarly, PeLEDs performance suffers from trap state-induced non-radiative energy transfer, leading to low photoluminescence (PL) quantum yields (QY) and short PL lifetimes.(Chen *et al.*, 2014) Therefore, attaining ultralow defective and impurity-free materials is necessary to achieve high performance for conventional semiconductor.(Brandt *et al.*, 2015)

In order to reduce the non-radiative energy transfer and obtain perovskites with high crystal quality, controllable (e.g. morphology and crystallinity) and low cost synthesis techniques have been examined by scientific area. To date, a number of synthesis methods have been reported such as ligand-mediated crystallization, hot injection,(Protesescu *et al.*, 2015) and antisolvent crystallization.(Schmidt *et al.*, 2014; Zhang *et al.*, 2015) In addition to their synthesis, the requirement of coating process to fabricate perovskite-based devices poses an additional step. In this context, single step strategies such as anti-solvent vapor treatment, polymer additive assisted film growth, precursor solution composition optimization,(Zhang *et al.*, 2017; Ban *et al.*, 2018; Yuan *et al.*, 2018; Wu *et al.*, 2017) hand spray coating,(Gamliel *et al.*, 2015; Ramesh *et al.*, 2015) and electrospraying has been developed to simultaneously fabricate the crystal and its thin layer. Among these methods, electrospraying offers an opportunity to achieve high purity, size and shape control and to lower the excessive usage of volatile chemical compounds.

Electrospraying is an all-purpose technique in which under an electric field between the tip and a grounded collector, fine liquid droplets are repelled from a sharp tip onto a metal or metal-supported substrate for coating.(Kumar *et al.*, 2014) Naphade *et al.* reported an approach for the synthesis of low-dimensional MAPbX₃-based perovskite colloidal nanostructures in a single step by combining anti-solvent solvent extraction technique with the electrospraying process.(Naphade *et al.*, 2015) The handicap of this process is that the anti-solvent bath in a metal electrode container is used as collector instead of a solid substrate. Therefore, one can require to perform some further steps such as centrifugation, dispersing and spin-coating or drop-cast, etc in order to apply perovskites on the desired substrate for device application. In another study, Hong *et al.* proposed a technique that enables uniform perovskite coatings on hot substrates by electrospray coating system.(Hong *et al.*, 2017) However, heating the collector requires extra energy and increases the cost of fabrication.

On the other hand, apart from studies in perovskite nanocrystals, it has been shown that nanoscale materials may present unique characteristics due to the dimensional reduction. In the last two decades, discovery of graphene, has increased the interest in atomically thin two-dimensional (2D) materials that are suitable candidates for ultrathin flexible optoelectronic devices.(Novoselov *et al.*, 2004) Soon after, the studies on 2D materials such as hexagonal boron nitride (h-BN),(Han *et al.*, 2008) MoS₂,(Radisavljevic *et al.*, 2011) transition metal dichalcogenides (TMDs),(Neto and Novoselov, 2011; Mak *et al.*, 2010; Splendiani *et al.*, 2010; Wang *et al.*, 2012) and alkaline-earth-metal hydroxides (AEMHs)(Aierken *et al.*, 2015) indicated that reduction in number of layers from bulk to monolayer leads to significant changes in vibrational, optical and electrical properties. Following these advances, the interest in thickness dependent properties of organic, hybrid and MAPbX₃ perovskites which are suitable candidate for optoelectronic applications has started to increase and recent studies proved that also cesium lead halide perovskites' optical, electronic and vibrational properties may vary with their thickness.(Sichert *et al.*, 2015; Tyagi *et al.*, 2015; Dou *et al.*, 2015; Hassan *et al.*, 2016)

Among cesium lead halide perovskites, cubic phase (α -CsPbI₃) show high thermal stability and excellent photoluminescence properties with a bandgap of 1.73 eV which is desirable for optoelectronic device applications.(Sutton *et al.*, 2016; Kulbak *et al.*, 2015) Unfortunately, the phase transition is inevitable for α -CsPbI₃ perovskites which are stable

at high temperature ($>320\text{ }^{\circ}\text{C}$)(Dastidar *et al.*, 2017) and at ambient conditions, the α - CsPbI_3 nanocrystals transform to the orthorhombic structure which is also called yellow-phase.(Sutton *et al.*, 2016; Eperon *et al.*, 2015) Although researches have been conducted the cubic CsPbI_3 to stabilize its structure, it has been found that the phase transition is inevitable and the orthorhombic phase is more favorable than the cubic phase at room temperature. Therefore, understanding this phase is a key point for dealing with cesium lead halide perovskites. However, there are very few studies(İyikanat *et al.*, 2017; Molina-Sánchez, 2018) on how the characteristic properties of cesium perovskites are modified going from their bulk to ultra-thin structures.

In this thesis, dimension dependent optoelectronic properties of cesium lead halide perovskites are investigated with optic, XRD measurements, STEM images and by means of state-of-the-art first-principles calculations. A novel and facile perovskite fabricating and coating approach by electrospraying method is introduced. By this method, color tunable inorganic perovskites films containing nanoplatelets is achieved. Their ligand (OAm) induced degree of quantum confinement is discussed. Moreover, it is investigated the dimensional reduction dependent structural, electrical, optical and vibrational characteristics of orthorhombic CsPbI_3 perovskite crystals. A detailed analysis, based on DFT simulations, for bulk and possible bilayer and single layer structures of CsPbI_3 are presented in detail. Lastly, it is observed that the red shift in photoluminescence peak of water interacted CsPbBr_3 nanowires arise from detachment of surface ligand from surface of nanowire by presense of water molecules.

CHAPTER 2

METHODOLOGY

2.1. Experimental Methodology

In this section, the experimental methodology is introduced as cesium lead halide perovskite synthesis and characterization techniques which are mainly used in this thesis.

2.1.1. Cesium Lead Halide Perovskite Synthesis

In this subsection, a detailed information about perovskite synthesis methods is given.

2.1.1.1. Hot-Injection Method

Cs-oleate Synthesis: In order to obtain Cs-oleate solution, OA ($625\mu\text{L}$), ODE (7.5 mL) and Cs_2CO_3 (0.2 g) were mixed in 3 necked flask at 120°C , under vacuum (150 mbar) dried for 1h.(Amgar *et al.*, 2017) Yellowish Cs-oleate solution was slowly cooled off.

CsPbBr₃ Synthesis: In a few steps with minor alterations based on procedure,(Amgar *et al.*, 2017) CsPbBr₃ crystals were obtained. 1.25 ml ODE, 0.125 mL OLA and 0.125 mL OA mixture was filled to a vial. 0.1 mL of pre-heated Cs-oleate solution and 0.2 mL of PbBr₂ precursor solution were respectively added to this mixture. After 10 s, in order to cause the CsPbBr₃ to crystallize 5 mL acetone was quickly added. After 30 minutes stirring and by centrifugation (6000 rpm, 10 m) crystallized green precipitates were obtained and finally these crystallized precipitates were dispersed in hexane.

2.1.1.2. Electrospraying Method

Preparation of Precursor Solution: The precursor solution was prepared by following the method proposed by Li *et al.* (Li *et al.*, 2016) CsBr (0.4 M), PbBr₂ (0.4 M) and DMF (10 mL) are loaded into a 20 ml glass vial and mixed via magnetic stirrer. After full dissolution of the salts, desired amount of OA and OAm are added to the solution under vigorous stirring.

Fabrication of CsPbBr₃ Thin Films: An aliquot of the precursor solution (0.4 mL) was loaded into a plastic syringe with an inner diameter of 1.3 mm. For electrospaying by electric field between stainless-steel needle (21Gx1 1/2, Interlab) and ITO coated glass ($R_s < 10 \Omega/\text{sq.}$, Teknoma), the electric voltage was applied from 5 to 20 kV by DC power supply (Gamma H. V. Research Ormand Beach, FL). The flow rate was controlled between 0.25 and 1.5 mL/h by a programmable syringe pump (SyringePump, NE-1000). The distance between the needle and ITO substrate was fixed to 16 cm.

2.1.2. Characterization Techniques

In this subsection, mainly used characterization techniques are discussed such as UV-Vis Absorption Spectroscopy, Photoluminescence and Raman Spectroscopy.

2.1.2.1. UV-Vis Absorption Spectroscopy

It is extensively used to examine a semiconductor's band structure with optical transmission or absorption spectrum. A material's band gap energy is the lowest amount of energy the material needs to excite an electron from the valance band (VB) to the conduction band (CB) by absorbing a photon. More energetical photons than band gap energy of the material excite electrons. This process is called as absorption. However, low energetical photons than the band gap are transmitted through the material, for semiconductors. However, semiconductors are seperated into two type of material as direct band gap or indirect band gap semiconductor. Materials exhibit various properties depending on the type of band gap. The absorption coefficient was calculated using the relation:

$$\alpha = \ln[(1 - R(\lambda))/T(\lambda)]/d \quad (2.1)$$

where T is transmittance and R is reflectance. The α is the absorption coefficient and d is the thickness of the sample. Absorption properties of a semiconductor have a large impact on the materials functionality in light-sensors, solar cells etc. applications. The absorption coefficient helps to evaluate thin film optical band gap. By performing Tauc plot of absorption coefficient, the optical band gap or Tauc gap of semiconductor may be able to obtained from intersection of plot with x-axis. The equation of Tauc plot is given as:

$$\alpha h\nu = A(h\nu - E_g)^r \quad (2.2)$$

where $h\nu$ is incident photon energy, A is a constant, E_g is band gap and r changes depending on the material type.

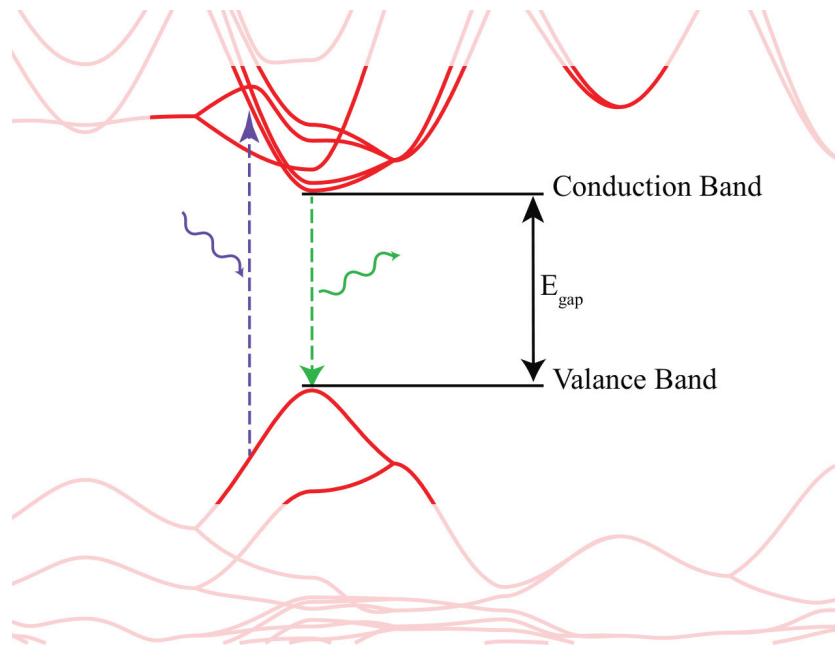


Figure 2.1. Absorption and emission of photon schematic.

2.1.2.2. Photoluminescence

Luminescence is a spontaneous emission of light from a substance, not produced by heat. Therefore, it is a sort of cold-body radiation. It is also a non-destructive characterization which is crucial in order to determine the fundamental optical properties of materials for optoelectronic device applications.

Photoluminescence (PL) which is the most common non-destructive technique among the luminescence spectroscopies, is used to specify the point defects or to measure the materials' band gap. Photoluminescence is a term that covers fluorescence and phosphorescence. Fluorescence is the emission of electromagnetic radiation (mostly visible light) caused by the immediate relaxation of the excited atoms in a material. It is an almost instantaneous process that happens in about 10^{-8} second. On the other hand, phosphorescence is also emission of electromagnetic radiation originated from the excited atoms in a material. But unlike fluorescence, in this process, an intermediate level of energy which is called as metastable state or electron trap state, is interposed between ground state and excited state. After an excited electron falls into the metastable state so it takes about 10^{-3} second to hours or years, depending on the circumstances.

An electron is excited from valance band to conduction band and electron-hole pair is created, when a photon is absorbed by a semiconductor. The excited electron desires to relax to its ground state. Recombination process of electron-hole pairs occurs in two possible ways, non-radiative or radiative transitions. Radiative transition means that the material produces a photon of a specific energy that corresponds to its band gap semiconductor like perovksites. The produced photon can be originated from defect sites or crystals of the material. On the other hand, there are few non-radiative transition ways such as phonon-induced and Auger processes.

Our Optical Measurement Setup :

In this thesis, optical measurements were carried out by using home made Ocean Optics setup.

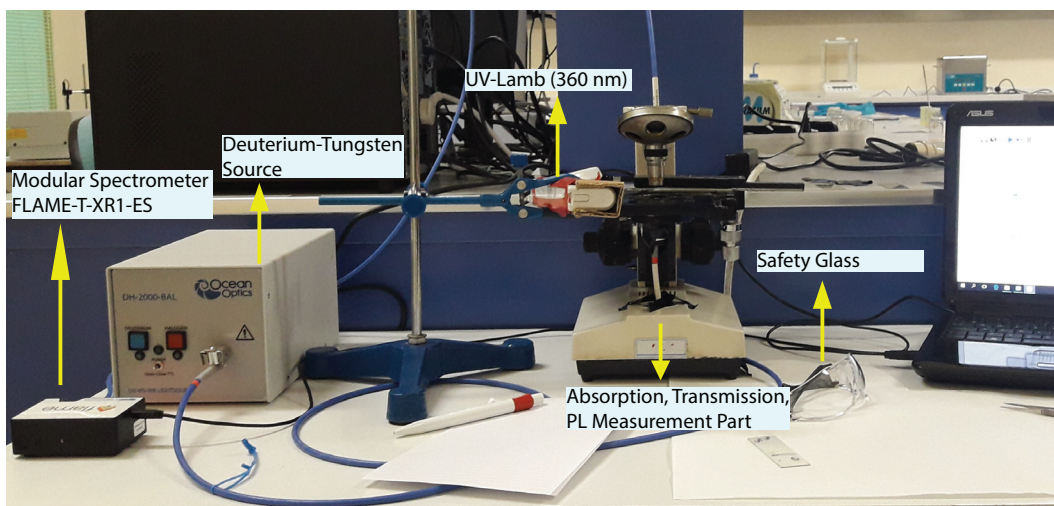


Figure 2.2. Optic Measurement setup in the Cent Lab.

2.1.2.3. Raman Spectroscopy

Raman spectroscopy is a light scattering spectroscopy technique which is used in order to obtain information about the vibrational and rotational modes of materials. Therefore, chemists, physicists and material scientists are traditionally using this technique in the laboratories as a means of determining the chemical structure of materials. Generally speaking, the technique involves examining a spectrum of scattered light that presents certain light intensity peaks attributed to the crystal structure of the material. This technique uses the unique Raman spectra to define unknown samples or even further analysis based on information from the spectrum as a spectral "fingerprint" for various components.

When electromagnetic waves interact with samples (atom, molecules, etc.), light redirection can be considered the light scattering. As a result of the interaction between the electromagnetic waves and sample, electrons are periodically disturbed at the same frequency (ν_0), thus generating a dipole electrical moment induced in the electrical field and the scattered light propagates due to this electronic cloud disturbance. Furthermore, scattered photons most likely will have the same energy as the incident photon. This process is known as elastic scattering which is also called as 'Rayleigh scattering'. On the other hand, some of the scattered photons will have a different frequency compared

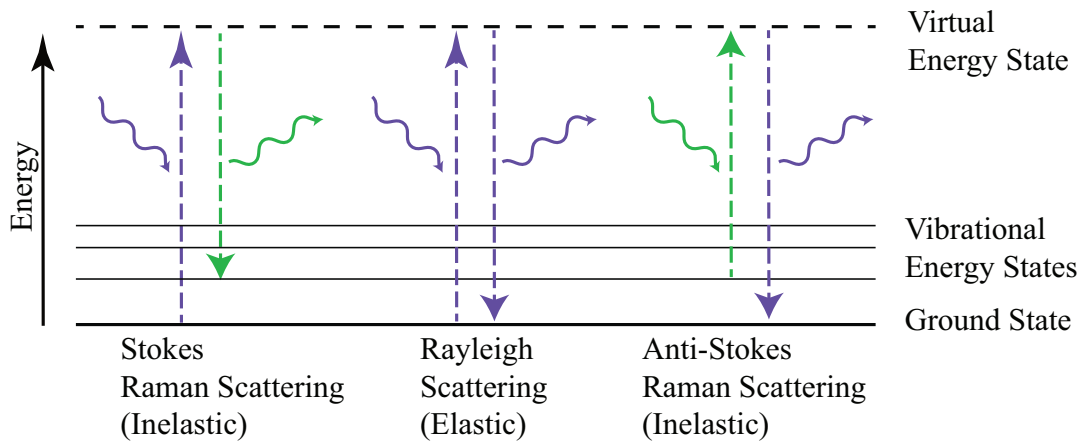


Figure 2.3. Quantum energy transitions for Rayleigh and Raman scattering.

to incident photon. This process is known as inelastic scattering or Raman scattering. However, inelastic scattering is very a rare process which happens in every 10^{-7} scattering process.

Inelastic scattering process is also divided into two processes as Stokes scattering in which scattered photons have higher energy than that of incident photons, and anti-Stokes scattering which refers that the scattered photons have lower energy than the incident photons. Most of the scattering atoms of the substrate remain in their ground states and they need to be in excited states in order to obtain anti-Stokes shift. So it is observed that the number of Stokes shift processes much higher than the number of anti-Stokes shift processes.

Our Raman Spectroscopy Setup :

In this thesis, the Horiba Xplora Plus Raman system is used in order to conduct Raman measurements. Synergicity grating spectrometer is included in the system with choosable holographic and sensitive from the near IR to near UV region four gratings of 600 grooves(gr)/mm, 1200 gr/mm, 1800 gr/mm, and 2400 gr/mm. For sample excitation 532 nm and 785 nm lasers are used. Laser light is first filtered from the plasma lines, then directed to a beam-splitter after a set of neutral (ND) filters is passed over. The beam splitter (BS) transmits some part of the light from top to bottom through an Olympus BX51 optical microscope. The laser light is focused on the sample surface by passing

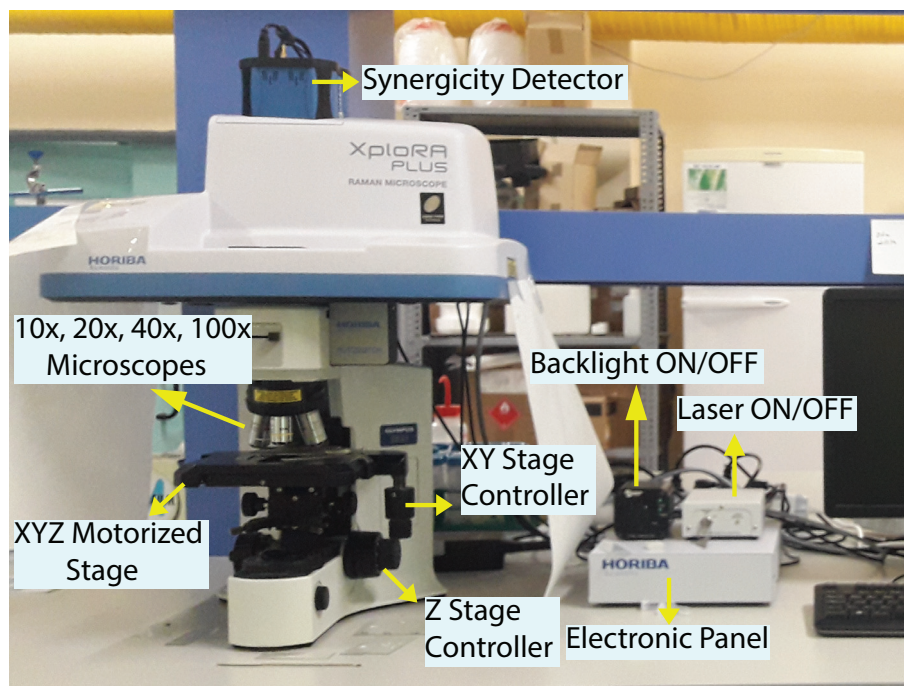


Figure 2.4. Horiba Xplora Plus Raman system in the Cent Lab.

through an suitable objective (10x, 20x, 50x, or 100x). (The minimum spot size on a smooth sample surface is approximately 1 micron with 100x objective)

In the back-scattering geometry, a scattered light is collected by the same microscope objective from the sample mounted on an XYZ stage, with full computer and hand control in all directions. There is a set of three Rayleigh rejection notch filters with wavelengths of 785 and 532 nm between BS and the monochromator entrance slit which are chosen by the computer to block the particular wavelength of excitation. In the monochromator, light is detected by the synergicity detector (CCD detector) and sent to the controlling computer as data signal for analysis.

2.2. Computational Methodology

In this section, a brief information about the density functional theory (DFT) is given. DFT were mostly used in order to obtain ground state energies, electronic and vibrational band diagrams of the systems.

2.2.1. Density Functional Theory

Density functional theory (DFT) is a computational quantum mechanical modelling method. In this subsection, origins of the DFT are discussed.

2.2.1.1. Basics of Density Functional Theory

The properties of a system (many-electron) can be achieved through the solution of the quantum mechanical wave equation that governs system dynamics. This is simply Schrödinger's equation for non-relativistic systems. However, for researchers some of the most remarkable challenges in quantum mechanics are generated by many-electron systems in order to understand such systems in many applications. Density functional theory (DFT) is the most practical and popular method by using quantum mechanical solutions in order to solve this complicated system.

DFT is the most popular quantum mechanical way of determining the structural, electronic, magnetic, mechanical, vibrational and optical properties of materials. DFT simply establishes that a functional of the ground state density which is a function of position, can be written for interacting many-particle system. DFT becomes the most widely used technique because all the physical ground state properties of materials can be defined as functional of a ground state density.

All physical information is stored in the wave function. The time-dependent non-relative Schrödinger equation can be the mathematical illustration of such a wave function;

$$\hat{H}\Psi = E\Psi \quad (2.3)$$

where the operator \hat{H} is the energy operator known as the Hamiltonian and the E is the corresponding eigenvalue for the Hamiltonian operator in Schrödinger equation. The eigenfunctions of the Schrödinger equation which are the wave function Ψ , are the solutions of Eq. 2.3. It's almost unsolvable the Eq 2.3 if an N-body system is assumed, unless the quantum computer is used or without consideration of any approximations. The non-relativistic many-body \hat{H} has the general form as;

$$\hat{H} = -\frac{\hbar^2}{2m_e} \sum_i^N \nabla_i^2 + \frac{e^2}{4\pi\epsilon_0} \left[-\sum_i^N \sum_I^N \frac{Z_I}{|\vec{r}_i - \vec{R}_I|} + \frac{1}{2} \sum_i^N \sum_{j \neq i}^N \frac{1}{|\vec{r}_i - \vec{r}_j|} + \frac{1}{2} \sum_i^N \sum_{J \neq I}^N \frac{Z_I Z_J}{|\vec{R}_I - \vec{R}_J|} \right] \quad (2.4)$$

for N-body systems which contains M nuclei and N electrons.

The system's kinetic energy is included in the first two terms with electrons and nuclei. The third term is the Coulomb repulsion term between electrons and fourth one is the Coulomb repulsion term between nuclei. Lastly, the final term is the Coulombic interaction between an electron and nuclei. The ∇_i^2 and ∇_A^2 are Laplacian operators in the coordinates of electron and nuclei, respectively.

2.2.1.2. Hohenberg-Kohn Theorems

Hohenberg and Kohn first introduced the approach which demonstrates that a quantum many-body system's ground state can be regarded as a remarkable density functional that makes DFT relevant, in 1964. The approach represents two main theorems; (i) The external potential is a unique density functional for any system of interacting particles in an external potential $V_{ext}(\mathbf{r})$, (ii) The total energy ($E[n]$) can be described in terms of the density for the energy. The functional which supplies the system's ground-state energy provides the minimum energy if the input density is the true ground-state density. The density of electron $n_0(\mathbf{r})$ of the ground state can be determined with a principle of variation. Then the total energy functional for a particular V_{ext} becomes as,

$$E = \frac{\langle \Psi_0 | H | \Psi_0 \rangle}{\langle \Psi_0 | \Psi_0 \rangle} \equiv \langle H \rangle = \langle T \rangle + \int d^3\mathbf{r} V_{ext}(\mathbf{r}) n_0(\mathbf{r}) + \langle V_{int} \rangle + E_{II} \quad (2.5)$$

2.2.1.3. Hellmann-Feynman Theorem

Hellmann-Feynman Theorem states that the expectation value of the derivative of the Hamiltonian in terms of a parameter can be found by derivative of the total energy with respect to the same parameter. By solving the Schrödinger equation if the spatial

distribution of the electrons are obtained, all forces which are in terms of kinetic energy and the charge density of the electron exchange and correlation, in this system can be calculated. Therefore, it is crucial for structural optimizations in DFT calculations.

$$\mathbf{F}_I = -\frac{\partial E}{\partial \mathbf{R}_I} \quad (2.6)$$

where the force depends only on the density of electrons, n , and the other nuclei. When we consider the total energy expression in Eq. 2.5, the force can be written as

$$\mathbf{F}_I = -\frac{\partial E}{\partial \mathbf{R}_I} = -\int d^3\mathbf{r} n(\mathbf{r}) \frac{\partial V_{ext}(\mathbf{r})}{\partial \mathbf{R}_I} - \frac{\partial E_{II}}{\partial \mathbf{R}_I} \quad (2.7)$$

2.2.1.4. The Kohn-Sham Equations

Kohn-Sham presented a Hohenberg-Kohn theorem-based method that allows one to minimize the functional energy by differing the charge density over all densities containing N electrons. The energy functional given in Eq. 2.8 now takes the form,

$$E[n] = \int n(r)V_{ext}(r)dr + F_{HK}[n] = \int n(r)V_{ext}(r)dr + T[n] + E^{Hartree}[n] + E_{xc}[n] \quad (2.8)$$

where the universal functional, $F_{HK}[n]$, is written as the sum of kinetic energy of non-interacting electrons, $T[n]$, Hartree energy, $E^{Hartree}$, and exchange and correlation energy, E_{xc} . Here, the important step is defining an effective potential which is written as,

$$V^{eff} = \frac{\delta\{\int n(r)V_{ext}(r)dr + E^{Hartree}[n] + E_{xc}[n]\}}{\delta n(r)}, \quad (2.9)$$

which results in the form,

$$V^{eff} = V_{ext}(r) + \int \frac{n(r')}{|r-r'|} dr' + V_{xc}(r), \quad (2.10)$$

where $V_{xc}(r)$ is the exchange-correlation potential derived from the exchange-correlation energy. Using this form of effective potential, the Schrodinger equation in Kohn-Sham DFT takes the form of one-electron like equation as,

$$\left[-\frac{1}{2}\nabla^2 + V^{eff} \right] \phi_i = E_i \phi_i \quad (2.11)$$

where the eigenfunctions, ϕ_i , are known as the Kohn-Sham one-electron orbitals which result in the electron density,

$$n(r) = \sum_{i=1}^N |\phi_i|^2 \quad (2.12)$$

Due to the form of Eq. 2.12, the effective potential, V^{eff} , depends on the density, $n(r)$. Thus, the Kohn-Sham equation should be solved by the following way: (i) begin with an initial guess of the electron density, (ii) construct the effective potential, V^{eff} , by the knowledge of electron density, (iii) calculate the corresponding Kohn-Sham orbitals, ϕ_i , and (iv) calculate the new electron density corresponding to these orbitals and compare with the initial one.

2.2.1.5. Functionals of Exchange and Correlation

The exchange-correlation functional is necessary in order to solve the Kohn-Sham equation. But an exact expression is not available so an approximation must be established. Two most common approximations which are widely used in DFT calculations, such as LDA (Local Density Approximation) and GGA (Generalized Gradient Approximation) are explained.

Local Density Approximation (LDA) :

According to local density approximation (LDA), the exchange correlation energy can be considered the same as the energy exchange correlation functional of a locally uniform electron gas where the charge density is slowly varying.

Despite the basic approximation, LDA provides very reliable results (especially for bulk materials) and forms the core of DFT codes. Even in systems where the charge density varies rapidly, it works fairly well and LDA works particularly well for metallic systems. However, atomic ground-state energies and ionization energies are undervalued within this approximation, while binding energies are overestimated.

Generalized Gradient Approximation (GGA) :

In this approximation, the gradient of the electron density is introduced because of the inadequacy of LDA for variety materials that have rapidly varying electron density. Due to its dependence on the gradient of the electron density, GGA functionals are known as semi-local functionals.

2.3. Vasp Input Set

This section introduces the general computation methodology which we used to study systems considered and discussed in following chapters. The details for the particular system is given in the corresponding chapter. Our investigations on the structural, electronic, properties of the ultra-thin materials considered were carried out using the VASP software. The VASP code solves the Kohn-Sham equations (Kohn and Sham, 1965) iteratively for a system with periodic boundary conditions using plane-wave basis set. In order to describe the electron exchange and correlation, the local density approximation (LDA) was adopted.(Perdew and Zunger, 1981) The spin-orbit interaction, which is essential for some materials (especially for atoms having larger radius), was included in the calculations. To obtain the charge distribution on the structures, Bader technique was used.(Henkelman *et al.*, 2006)

Structural optimizations were performed by using following parameters. The energy cutoff of the plane-wave basis set was taken to be 500 eV for all calculations. In order to minimize the total energy, the energy difference between the sequential steps was set to 10^{-5} eV. The convergence for the total Hellmann-Feynman forces in the unitcell was taken to be 0.05 eV/Å. In addition, for self-consistent calculations, width of the of the Gaussian smearing of 0.05 eV was used. The pressures on the unit cell were reduced to 1.0 kB in three directions. For the determination of accurate charge densities, Brillouin Zone integration was performed using dense Γ -centered k -point samplings.

CHAPTER 3

COLOR TUNABLE ALL-INORGANIC PEROVSKITES SYNTHESIZED BY ELECTROSPRAYING

Herein, we demonstrate a novel coating approach to fabricate CsPbBr₃ perovskite nanoplatelet film with heat-free process via electrospaying from precursor solution. A detailed study is carried out to determine the effect of various parameters such as ligand concentration, electric field, flow rate etc. on the optical properties. By controlling the volume ratios of the oleylamine (OAm) and oleic acid (OA), the coalescing and thickness of the resulting nanoplatelets can be readily tuned that results in control over emission in the range of 100 nm without any anti-solvent crystallization or heating processes. The varying electrical field and flow rate was found as inefficient on the emission characteristics of the films. In addition, the crystal films were obtained under ambient conditions on the ITO coated glass surfaces as in the desired pattern. As a result, we demonstrated a facile and reproducible way of synthesizing and coating of CsPbBr₃ perovskite nanoplatelets which is suitable for large-scale production. In this method, the ability of tuning the degree of quantum confinement for perovskite nanoplatelets is promising to fabricate wide variety of optoelectronic devices.

All-inorganic cesium lead halide perovskites (ILHPs) have attracted tremendous attention in recent years. Due to their extraordinary optical peculiarities, ILHPs are gaining wide variety of role as strong contenders in optoelectronic research with tunable band-gap, large absorption cross-section, long carrier lifetime, and high carrier mobility. (Protesescu *et al.*, 2015; Akkerman *et al.*, 2015; Makarov *et al.*, 2016; Stranks *et al.*, 2013) Therefore, the fabrication of ILHP nanostructures with controllable composition, morphology, dimensionality, and orientation has become important as the main focus, to employ the perovskites' superior properties in photovoltaics.

Since their applicability in photovoltaics including solar cells and light-emitting diodes (LEDs) the fabrication methods of perovskite thin films with desired shape and size is crucial. For instance, the large crystal size or grain boundaries decrease the electroluminescence (EL) performance of perovskite light-emitting diodes (PeLEDs) because

of trap states.(Cho *et al.*, 2017; Wei *et al.*, 2016; Pan *et al.*, 2016) The probability for non-radiative recombination in large-sized crystals mostly increases, which results in a low EL efficiency for PeLEDs.(Kim *et al.*, 2016; Cho *et al.*, 2015) Similarly, PeLEDs performance suffers from trap state-induced non-radiative energy transfer, leading to low photoluminescence (PL) quantum yields (QY) and short PL lifetimes.(Chen *et al.*, 2014) Therefore, attaining ultralow defective and impurity-free materials is necessary to achieve high performance for conventional semiconductor.(Brandt *et al.*, 2015)

In order to reduce the non-radiative energy transfer and obtain perovskites with high crystal quality, controllable (e.g. morphology and crystallinity) and low cost synthesis techniques have been examined by scientific area. To date, a number of synthesis methods have been reported such as ligand-mediated crystallization, hot injection,(Protesescu *et al.*, 2015) and antisolvent crystallization.(Schmidt *et al.*, 2014; Zhang *et al.*, 2015) In addition to their synthesis, the requirement of coating process to fabricate perovskite-based devices poses an additional step. In this context, single step strategies such as anti-solvent vapor treatment, polymer additive assisted film growth, precursor solution composition optimization,(Zhang *et al.*, 2017; Ban *et al.*, 2018; Yuan *et al.*, 2018; Wu *et al.*, 2017) hand spray coating,(Gamliel *et al.*, 2015; Ramesh *et al.*, 2015) and electro spraying has been developed to simultaneously fabricate the crystal and its thin layer. Among these methods, electro spraying offers an opportunity to achieve high purity, size and shape control and to lower the excessive usage of volatile chemical compounds.

Electro spraying is an all-purpose technique in which under an electric field between the tip and a grounded collector, fine liquid droplets are repelled from a sharp tip onto a metal or metal-supported substrate for coating.(Kumar *et al.*, 2014) Naphade *et al.* reported an approach for the synthesis of low-dimensional MAPbX₃-based perovskite colloidal nanostructures in a single step by combining anti-solvent solvent extraction technique with the electro spraying process.(Naphade *et al.*, 2015) The handicap of this process is that the anti-solvent bath in a metal electrode container is used as collector instead of a solid substrate. Therefore, one can require to perform some further steps such as centrifugation, dispersing and spin-coating or drop-cast, etc in order to apply perovskites on the desired substrate for device application. In another study, Hong *et al.* proposed a technique that enables uniform perovskite coatings on hot substrates by electro spray coating system.(Hong *et al.*, 2017)

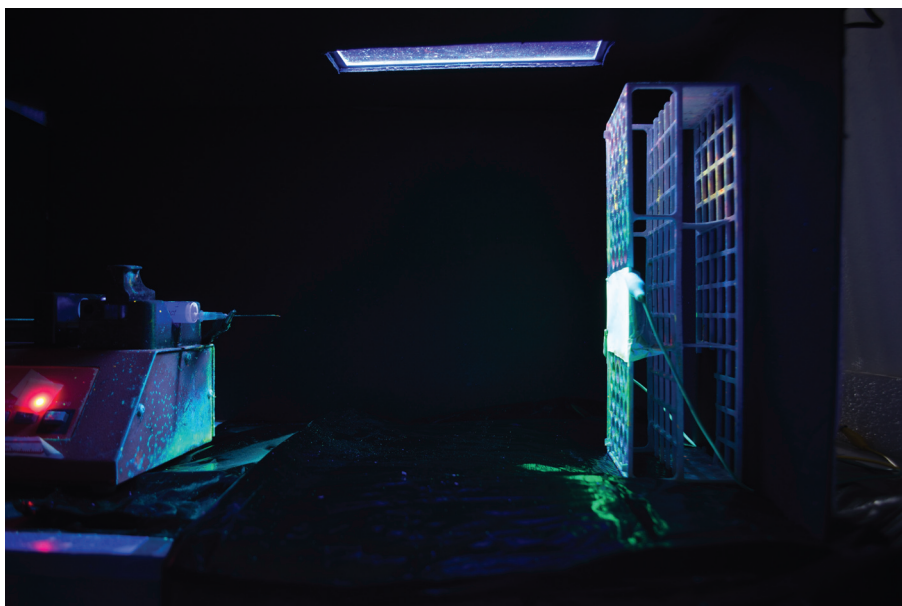


Figure 3.1. Photographic image of electrospaying setup.

Cesium Bromide (CsBr, 99.99%, Sigma-Aldrich), lead(II) bromide (PbBr_2 , $\geq 98\%$, Sigma-Aldrich), oleic acid (OA, 90%, Alfa Aesar), oleylamine (OAm, 90%, Sigma-Aldrich), N,N-dimethylformamide (DMF, $\geq 99.9\%$, Tekkim) were purchased and used as received without any further purification.

The precursor solution was prepared by following the method proposed by Li *et al.* (Li *et al.*, 2016) CsBr (0.4 M), PbBr_2 (0.4 M) and DMF (10 mL) are loaded into a 20 ml glass vial and mixed via magnetic stirrer. After full dissolution of the salts, desired amount of OA and OAm are added to the solution under vigorous stirring.

An aliquot of the precursor solution (0.4 mL) was loaded into a plastic syringe with an inner diameter of 1.3 mm. For electrospaying by electric field between stainless-steel needle (21Gx1 1/2, Interlab) and ITO coated glass ($R_s < 10 \Omega/\text{sq.}$, Teknoma), the electric voltage was applied from 5 to 20 kV by DC power supply (Gamma H. V. Research Ormand Beach, FL). The flow rate was controlled between 0.25 and 1.5 mL/h by a programmable syringe pump (SyringePump, NE-1000). The distance between the needle and ITO substrate was fixed to 16 cm (Fig. 3.1).

Optical characterizations including photoluminescence and absorption were obtained by USB2000+ Spectrometer (Ocean Optics Inc., Dunedin, FL, USA) via a pre-

mium fiber cable. The diffraction profile of the CsPbBr₃ structures was recorded with an X-ray diffractometer (XRD, XPert Pro, Philips, Eindhoven, The Netherlands). Scanning transmission electron microscopy (STEM; Quanta 250, FEI, Hillsboro, OR, USA) was used to determine the morphology of crystals via STEM detectors. In the case of STEM characterization, the samples are dispersed in the hexane and the colloidal dispersion in hexane was drop-casted on Formvar reinforced copper grids and dried in a vacuum.

The solidified nanocrystals were grown on an ITO substrate by the electro-spraying method. Spraying of the solution can be achieved only above particular electrical bias since the applied potential is required to overcome the surface tension of the precursor droplets. Eventually, the solution reaches to the needle head and directly wells out as a jet to grounded substrate, namely ITO. The accelerated droplets through the electric field transforms from liquid state into solid state forming crystals due to evaporation. Consequently, the crystals were deposit onto ITO when they reach the substrate. In this wise, the crystallization can be readily controlled by changing ligand fraction or electro-spraying experimental parameters such as solvent ratio, applied voltage and flow rate. In order to achieve full control over crystal geometry, in various amount of OAm was employed all of the electro-spraying processes due to its ability of intercalation between the thin layers of PbBr₂ octahedra. Therefore, OAm intercalation can lead to isolation of 2D perovskite nanoplatelets. The effect of OAm was investigated in the presence of OA.

3.1. Thickness Tunable Nanoplatelet Growth

In order to observe the effect of OAm, various amount of OAm was mixed to the precursor solution having 500 μ L of OA. The precursor solution was electro-sprayed onto the ITO substrate under electric potential (20 kV). As a result of the processes, the perovskite films were obtained with a various optical properties. Appearance of the films under both daylight and UV light (254 nm) is presented in Fig. 3.2 (a). A long-range control on emission characteristics from green to dark blue is achieved as a function of OAm in the precursor solution. The images reveal that the lack of OAm leads to form non-emissive larger crystals showing intense orange color (first images from right). As the perovskite crystal grows, it becomes more defect tolerant.(Kang and Wang, 2017) Due to formation of highly defective crystals, emission lifetime increases which results

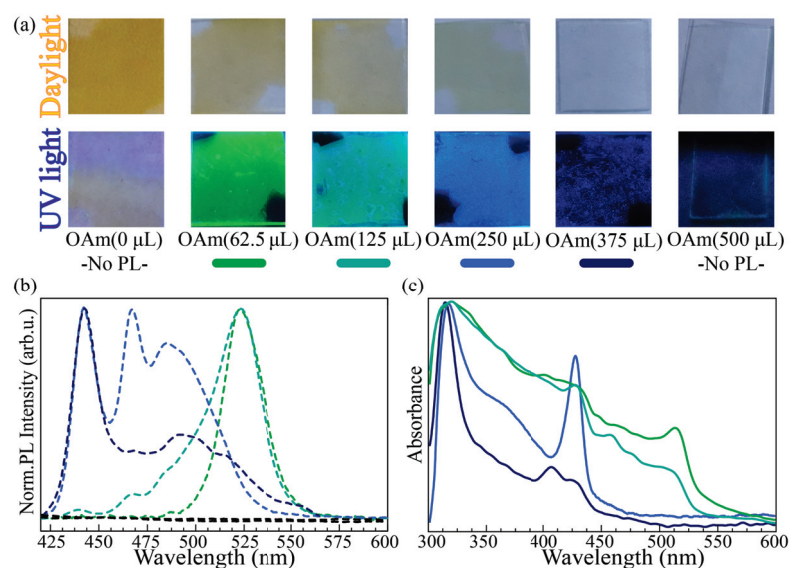


Figure 3.2. (a) Photographic image under daylight and under 254 nm UV light, (b) photoluminescence and (c) absorption spectra of perovskite films according to the amount of OAm in the presence of oleic acid (500 μ L).

in non-emissive behaviour. Therefore, it is observed that the opacity of the films gradually decreases as OAm fraction increases. On the other hand, excessive amount of OAm causes lack of emission due to passivation of crystal growth. The optical properties (PL, absorption) of corresponding films are presented in Fig. 3.2 (b) and (c). By decreasing the amount of OAm, sharp absorption peak at 430 nm that is attributed to the thin nanoplatelets, gradually fades away (Fig. 3.2 (b)).(Nasilowski *et al.*, 2016; Hong *et al.*, 1992a) Moreover, it is also observed that according to the amount of intercalation agent (amount of OAm), the photoluminescence characteristics of the films distinctly varies. The use of OAm with 375 uL leads to sharp signals at 436 and 464 nm and broad ones at 482, 493, and 525 nm nm in PL spectrum. As the amount of OAm decreases, the weak signals start to emerge towards 525 nm and intensity of high energetical peaks decrease. The behavior of relative intensities of PL peaks and absorption spectra hint about the thickening of the nanoplatelets by coalescing of nearby counterparts.(Weidman *et al.*, 2016; Shamsi *et al.*, 2016; Tong *et al.*, 2016; Yuan *et al.*, 2016) PL spectra suggest that the majority of PL intensities switch between high energetical (blue) and low energetical (green) regions by changing the OAm volume in the precursor solution.

The OAM molecules act as intercalation agent that binds to desired surface and creates a barrier against the coalescing of nanoplatelets. Hence, it results in 2D nanoplatelets and preservation of quantum confinement. (Sichert *et al.*, 2015; Yang *et al.*, 2018) The experimental results point out that the effect of OAM on emission characteristics, therefore crystal growth is passivated.

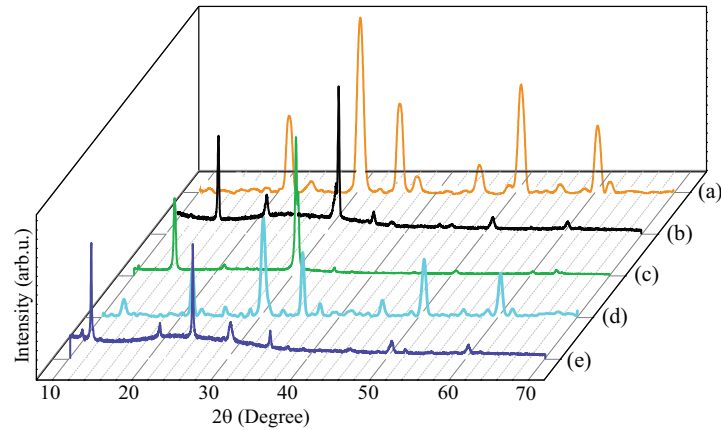


Figure 3.3. XRD diffractograms of (a) bare ITO substrate, (b) non-emissive, (c) green emitting, (d) cyan emitting, and (e) blue emitting perovskite films on ITO.

Further structural investigation was performed via X-ray diffraction (XRD) measurements, as shown in Fig. 3.3. Since the crystal films are collected on ITO substrate, its diffraction pattern is barely recorded and presented in Fig. 3.3 (a). The 2θ reflections at 15° and 30° refer to (001) and (002) planes, respectively (JPDCS no. 01-075-0412) as seen in Fig. 3.3 (b, c). The diffraction patterns of green-emitting and non-emissive films correspond to the cubic phase of CsPbBr_3 crystal structure. On the other hand, it is observed that these characteristic reflections are disappeared and the new 2θ reflections gradually emerge at 11.5° , 12.6° , and 25° , as the fraction of OAM increases (Fig. 3.3 (d, e)). These new peaks at small angles may hint about the presence of perovskite nanoplatelet. (Bekenstein *et al.*, 2015; Yang *et al.*, 2018)

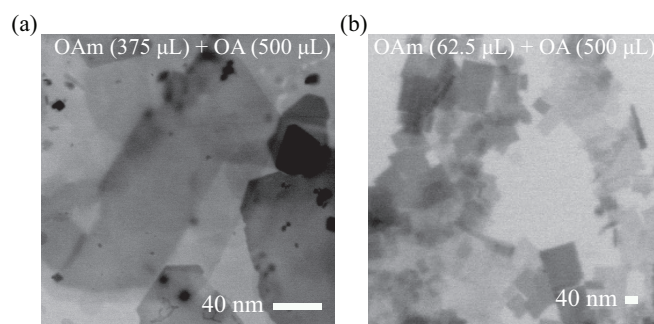


Figure 3.4. STEM images of (a) green emitting and (b) blue emitting perovskite films.

3.2. PL Evolution of Perovskite Nanoplakelet

For further structural examination, layered morphology of the crystals was investigated using STEM for dominantly blue and green emitting perovskite film as seen in Fig. 3.4 (a) and (b), respectively. STEM images were compared depending on the changing OAm fraction. Regional contrast differences are observed in the images, which indicate that the vertically stacked nanoplakelets vary in terms of thickness. Therefore, the stacking can influence the confinement, particularly. Note that the resulting perovskite films exhibit discrete emission peaks depending on the OAm fraction. In Fig. 3.2 (c), the energy difference between discrete PL maxima decreases as the layer thickness increases since the perovskite layer thickening causes a reduction in the degree of quantum confinement. As a result, these agreements also support the peak assignment of the resulting perovskite films. In general, nanoplakelets tend to form bulk crystals that can be prevented by using intercalation agent, namely OAm. Nevertheless, the use of a moderate amount of OAm cannot completely stabilize the crystals so that the nanoplakelets thicken, however, they cannot align on each other, perfectly. Hence, it results in non-homogeneous confinement, which leads to a number of discrete PL energy levels.

Furthermore, photoluminescence evolution was monitored in time for blue emitting perovskite film and given as a function of time (Fig. 3.5). It is observed that intense PL peak at 436 nm decreases in time and the relative intensities of 462, 480 and 515 nm PL peaks increase, respectively, in 24 hours. This result indicates that the nanoplakelets are slowly getting thicker. On the other hand, it also proves that the presence of perovskite

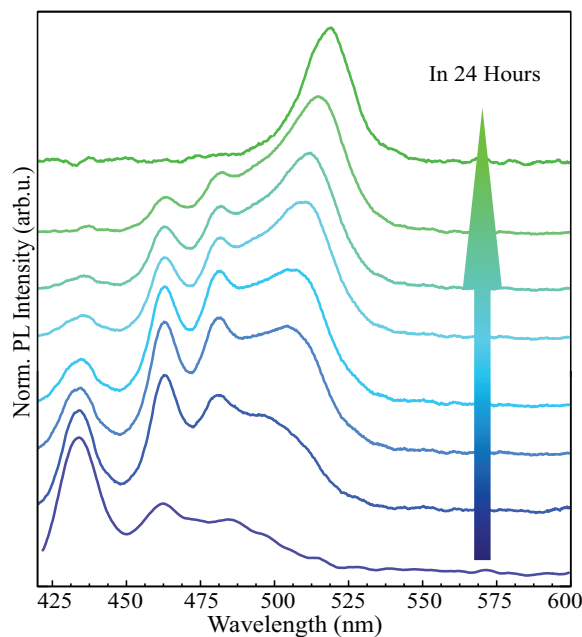


Figure 3.5. Time dependent PL evolution of blue emitting perovskite film under UV light.

nanoplatelets which are isolated from each other.

3.3. Effect of Electrospray Conditions

Furthermore, optoelectronic properties of the perovskite films were studied by changing electrospaying parameters such as voltage, flow rate, and solvent (DMF) fraction in precursor. In Fig. 3.6, the evolution of PL characteristics of 2D nanoplatelets is presented upon different parameters of electrospaying system with the 400 μL control precursor solution (OA-500 μL , OAm-250 μL).

In Fig. 3.6 (a) the PL spectra of the crystals that are obtained using different flow rates are presented. Varying the flow rate results in no change for PL peak positions. However, in the case of 0.25 ml/hr flow, the change in PL peak intensity is observed. The relative PL shifts toward low energetic region. Note that the process time increases as the flow rate decreases. Therefore, the coating process takes 96, 24 and 16 min, respectively, by using the same amount of precursor solution. Hence, the origin of the red shift in the

relative PL of 0.25 ml/hr is the exposure of crystals to ambient conditions for a longer time. It can be concluded that the optical properties of the films are unchanged as a function of flow rate.

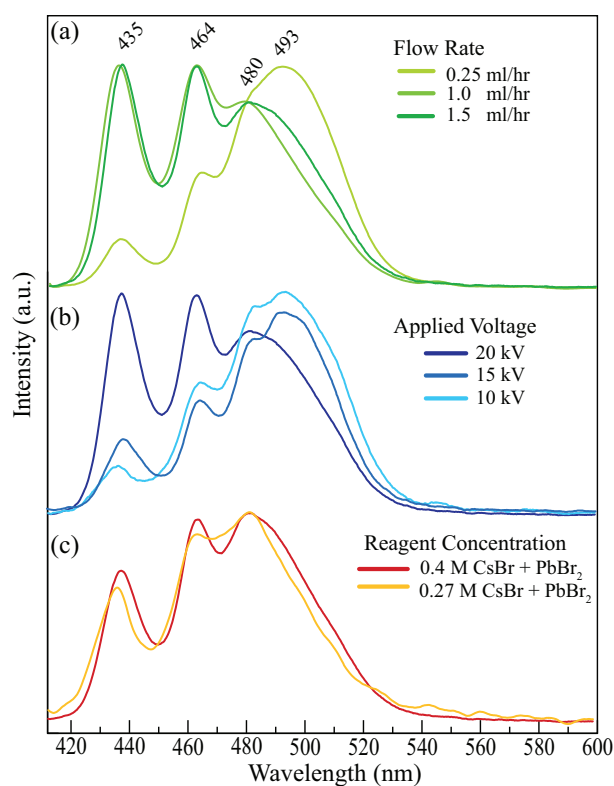


Figure 3.6. PL spectra of control sample with different (a) flow rate, (b) applied potential, and (c) reagent concentration.

On the other hand, in Fig. 3.6 (b), PL spectra of the resulting crystals are given for various potential differences. The potential difference controls the speed of electrospayed droplets, therefore, evaporation rate of DMF. It is observed that the most of droplets are unable to lose their liquid phase to form nanocrystals, in the case of 10 and 15 kV. The evaporation of the droplets is finished on ITO, which leads to formation of relatively larger crystals. Therefore, the peak at 493 nm appears more intensive. As the potential difference increases to 20 kV, the free-fly crystallization is achieved that results in more quantum confined perovskite film on the ITO.

Furthermore, as seen in Fig. 3.6 (c), relative PL behaviour is examined depending on the reagent concentration of precursor for normal (0.4 M CsBr + PbBr₂) and %33 lower

one. Resulting films show no any significant PL peak shifts or change due to number of ions per droplet.

Therefore, it is observed that electro spraying parameters and reagent concentration have no any effect on optoelectronic properties of perovskite nanoplatelets. However, it is achieved by only varying ligand ratios.

3.4. Lithography Performance of Electro spraying Method

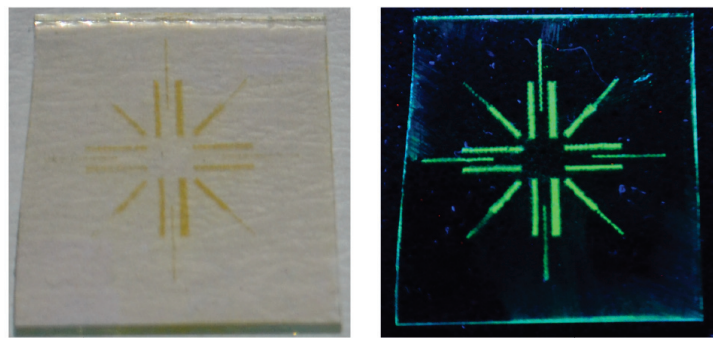


Figure 3.7. Patterned perovskite film on ITO, under daylight and UV light (254 nm).

For the manufacturing of integrated optoelectronic devices without losing functionality of the material, large area patterning is a crucial process. Due to their unique properties, a numerous techniques are used to fabricate optoelectronic devices using perovskites have been given a great deal of attention. Patterning is a big challenge for mass-production applications with perovskites which are solution-based soft materials. To fabricate the film in exact shape and pattern, polyethylene terephthalate (PET) made logo mask which is obtained by laser cut, was used. The mask was placed on ITO coated glass and patterned perovskite film was coated onto substrate via electro spraying. As seen in Fig. 3.7, it is confirmed that electro spraying method enables the direct patterning and synthesising of perovskite films with tunable optoelectronic properties in minutes. Additionally, it minimizes the fabrication-induced loss of the device.

CHAPTER 4

ORTHORHOMBIC CsPbI₃ PEROVSKITES: THICKNESS-DEPENDENT STRUCTURAL, OPTICAL AND VIBRATIONAL PROPERTIES

Cesium lead halide perovskites have been subject to intense investigation, mostly because of their potential to be used in optoelectronic device applications. However, regarding the need for nanoscale materials in forthcoming nanotechnology applications, understanding of how the characteristic properties of these perovskite crystals are modified through dimensional crossover is essential. In this study, thickness-dependence of the structural, electronic and vibrational properties orthorhombic CsPbI₃, which is one of the most stable phase at room temperature, is investigated by means of state-of-the-art first-principles calculations. The results show that (i) bilayers and monolayers of CsPbI₃ can be stabilized in orthorhombic crystal symmetry, (ii) among the possible ultra-thin perovskites only structures with CsI-terminated surface are dynamically stable (iii) electronic band gap increases with decrease in perovskite thickness due to quantum size effect and (iv) reflectivity and transmissivity of the orthorhombic CsPbI₃ can be drastically modified by tuning the thickness that modifies the electron confinement.

Among cesium lead halide perovskites, cubic phase (α -CsPbI₃) show high thermal stability and excellent photoluminescence properties with a bandgap of 1.73 eV which is desirable for optoelectronic device applications.(Sutton *et al.*, 2016; Kulbak *et al.*, 2015) Unfortunately, the phase transition is inevitable for α -CsPbI₃ perovskites which are stable at high temperature (>320 °C)(Dastidar *et al.*, 2017) and at ambient conditions, the α -CsPbI₃ nanocrystals transform to the orthorhombic structure which is also called yellow-phase.(Sutton *et al.*, 2016; Eperon *et al.*, 2015) Although researches have been conducted the cubic CsPbI₃ to stabilize its structure, it has been found that the phase transition is inevitable and the orthorhombic phase is more favorable than the cubic phase at room temperature. Therefore, understanding this phase is a key point for dealing with cesium lead halide perovskites. However, there are very few studies(İyikanat *et al.*, 2017; Molina-

Sánchez, 2018) on how the characteristic properties of cesium perovskites are modified going from their bulk to ultra-thin structures.

Density functional theory-based calculations were performed using the projector augmented wave (PAW)(Kresse and Joubert, 1999; Blöchl, 1994) potentials as implemented in the Vienna *ab initio* Simulation Package (VASP).(Kresse and Hafner, 1993, 1996) The exchange-correlation potentials are approximated by local density approximation (LDA).(Ceperley and Alder, 1980) In order to obtain the charge exchange between the ions,Bader technique was applied.(Henkelman *et al.*, 2006)

The frequency dependent dielectric function, $\epsilon(w) = \epsilon_1(w) + i\epsilon_2(w)$, of the materials was calculated by using the PBE0 functional on top of SOC. Using the dielectric function, other optical spectral quantities such as the absorption coefficient (α), reflectivity (R), and transmissivity (T) were calculated with the following formulas;

$$\alpha(w) = \sqrt{2}w \left\{ \left[\epsilon_1(w)^2 + \epsilon_2(w)^2 \right]^{1/2} - \epsilon_1(w) \right\}^{1/2} \quad (4.1)$$

$$R(w) = \left| \frac{\sqrt{\epsilon(w)} - 1}{\sqrt{\epsilon(w)} + 1} \right|^2 \quad (4.2)$$

$$T(w) = (1 - R(w))^2 e^{-\alpha(w)l} \quad (4.3)$$

where l is the thickness of the material.

4.1. Possible Structures of Ultra-thin Orthorhombic CsPbI₃

This section is devoted to investigation of the possible ultra-thin crystal structures of orthorhombic CsPbI₃ structure which is the frequently obtained product at room temperature.(Sutton *et al.*, 2018; Marronnier *et al.*, 2018) Crystal structures of the bulk and possible forms of bilayer and monolayer CsPbI₃ are shown in Fig.4.1.

Total energy optimization calculations reveal that optimized lattice parameters of bulk orthorhombic CsPbI₃ crystal are $a = 7.93 \text{ \AA}$, $b = 8.94 \text{ \AA}$, and $c = 12.21 \text{ \AA}$. As seen in the figure, CsPbI₃ crystal consists of PbI₆ octahedrals, which are tilted with respect to the cubic phase. Bader charge analysis shows that while Cs and Pb atoms donate 0.8 and 0.9 e , respectively while I atom receives 0.5 e .

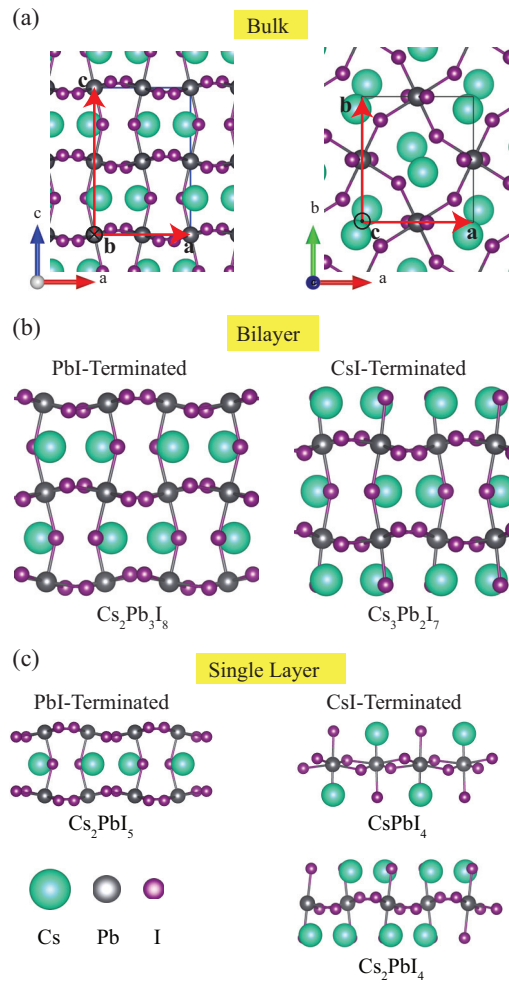


Figure 4.1. (a) Bulk, (b) bilayer, (c) monolayer structures of CsPbI_3 crystal.

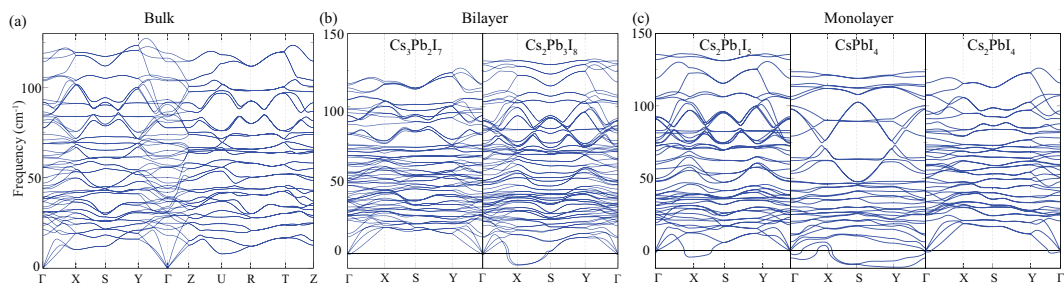


Figure 4.2. Phonon band diagram of (a) bulk CsPbI_3 crystal in orthorhombic phase, (b) $\text{Cs}_3\text{Pb}_2\text{I}_7$ and $\text{Cs}_2\text{Pb}_3\text{I}_8$ bilayers, (c) Cs_2PbI_5 , CsPbI_4 , and Cs_2PbI_4 monolayers.

In order to figure out the thickness dependent characteristics, we first examine bilayer structures derived from truncated bulk orthorhombic CsPbI₃. Therefore, two different bilayer configurations were derived from bulk material according to atom types forming the surface of the material. Obtained bilayer structures of Cs-I and Pb-I, shown in Fig. 4.1 (b), can be given by the chemical formula Cs₃Pb₂I₇ and Cs₂Pb₃I₈, respectively. The optimized lattice parameters of bilayer Cs₃Pb₂I₇ are $a = 7.62 \text{ \AA}$ and $b = 9.16 \text{ \AA}$ are obtained by structural analysis. The thickness of the bilayer Cs₃Pb₂I₇ is calculated to be 12.46 \AA . While surface and inner I atoms receive 0.6 and 0.5 e charge, respectively, each Pb and Cs atoms donate 0.8 e charge. Furthermore, the cohesive energy per atom of bilayer Cs₃Pb₂I₇ is found to be 3.13 eV is slightly smaller than that of the bulk structure (3.40 eV).

We complete the thickness-dependent structural analysis via scrutinizing the characteristics of the single layer form of the cesium lead iodide perovskite. As shown in Fig. 4.2 (c), there exist three possible structures when the material is thinned down to monolayer form. Depending on the atomic compositions, these monolayers can be presented by chemical formulas; Cs₂PbI₅, CsPbI₄, and Cs₂PbI₄. It is calculated that the optimized monolayer Cs₂PbI₄ lattice parameters are $a = 7.38 \text{ \AA}$ and $b = 9.28 \text{ \AA}$. Apparently, reduction of the thickness of the material leads to decrease in the a lattice parameter and increase in the b lattice parameter. However, the thickness of the monolayer Cs₂PbI₄ is found to be 6.30 \AA . Bader charge analysis reveals that each Cs and I atom donates 0.8 e charges to surface and inner I atoms receive 0.6 and 0.5 e charges, respectively. Following the trend that surface energy is increased by decreasing thickness, cohesive energy per atom of the monolayer Cs₂PbI₄ is reduced to 3.08 eV.

For understanding the vibrational properties and examination of the dynamical stability of CsPbI₃ phonon band dispersions of CsPbI₃, Cs₃Pb₂I₇, Cs₂Pb₃I₈, Cs₂PbI₅, CsPbI₄, and Cs₂PbI₄ are calculated (see in Fig. 4.2). Here small displacement methodology implemented in the PHONOPY code is used for the determination of elements of dynamical matrix and corresponding phonon spectrum. (Togo *et al.*, 2008) The phonon spectra of the bulk CsPbI₃ crystal exhibits real eigenvalues through all the symmetry points, confirming the dynamical stability of the structure and the reliability of the computational methodology.

It is seen from Fig. 4.2 that among the possible bilayers of orthorhombic CsPbI₃,

while the phonon spectrum of $\text{Cs}_3\text{Pb}_2\text{I}_7$ exhibits real eigenvalues through all the symmetry points, that of $\text{Cs}_2\text{Pb}_3\text{I}_8$ possesses imaginary eigenvalues in the large portion between the Γ and S high symmetry points. Therefore, it can be deduced that when the material is thinned down to its bilayers, only $\text{Cs}_3\text{Pb}_2\text{I}_7$ form is expected to be a stable.

Moreover, according to the phonon calculations, among the thinnest possible structures of orthorhombic CsPbI_3 , although single layer Cs_2PbI_5 and CsPbI_4 have a structure that is obtained by total energy optimization calculations, they cannot form dynamically stable crystal structures.

On the other hand Cs-rich form given by the formula Cs_2PbI_4 appears as the thinnest stable orthorhombic Cs perovskite. When going from bulk to single layers, cohesive energy decreases while the workfunction increases to 4.68 eV.

4.2. Electronic and Optical Properties of Ultra-thin CsPbI_3

To reveal the effect of dimensional reduction on the electronic properties of CsPbI_3 perovskite nanocrystals, electronic band dispersion calculations (by using LDA + PBE0 + SOC) are performed.

As shown in Fig. 4.3 (a), bulk CsPbI_3 is a semiconductor with a direct band gap of 1.9 eV. Both the conduction band minimum (CBM) and the valence band maximum (VBM) of the crystal reside at the Γ point. As seen in the previous work, (İyikanat *et al.*, 2017) contribution of the Cs atom in the material is negligible around the band edges. However, the VBM and CBM of the material are dominated by I-*p* and Pb-*p* orbitals. Fig. 4.3 (b) shows the electronic band dispersion for stable bilayer structure, $\text{Cs}_3\text{Pb}_2\text{I}_7$. Despite the thinning of the material and the presence of unbonded atoms on the surface, it is seen that the material still exhibits a direct bandgap at the Γ point. It is obtained that the thickness of the crystal decreases to bilayer form, the bandgap of the structure (2.6 eV) is almost 1.5 times of the bulk form (1.9 eV). It is also seen from Fig. 4.3 (c) that further decrease in dimension leads the significant increase in electronic energy band gap. Single layer Cs_2PbI_4 has a direct bandgap of 2.9 eV at the Γ point. Apparently, while the electronic dispersion characteristics remain unchanged with reduced thickness, the width of the bandgap is significantly enlarged. Therefore, one can also expect dramatical modifications in the optical properties of CsPbI_3 upon dimensional reduction. As repre-

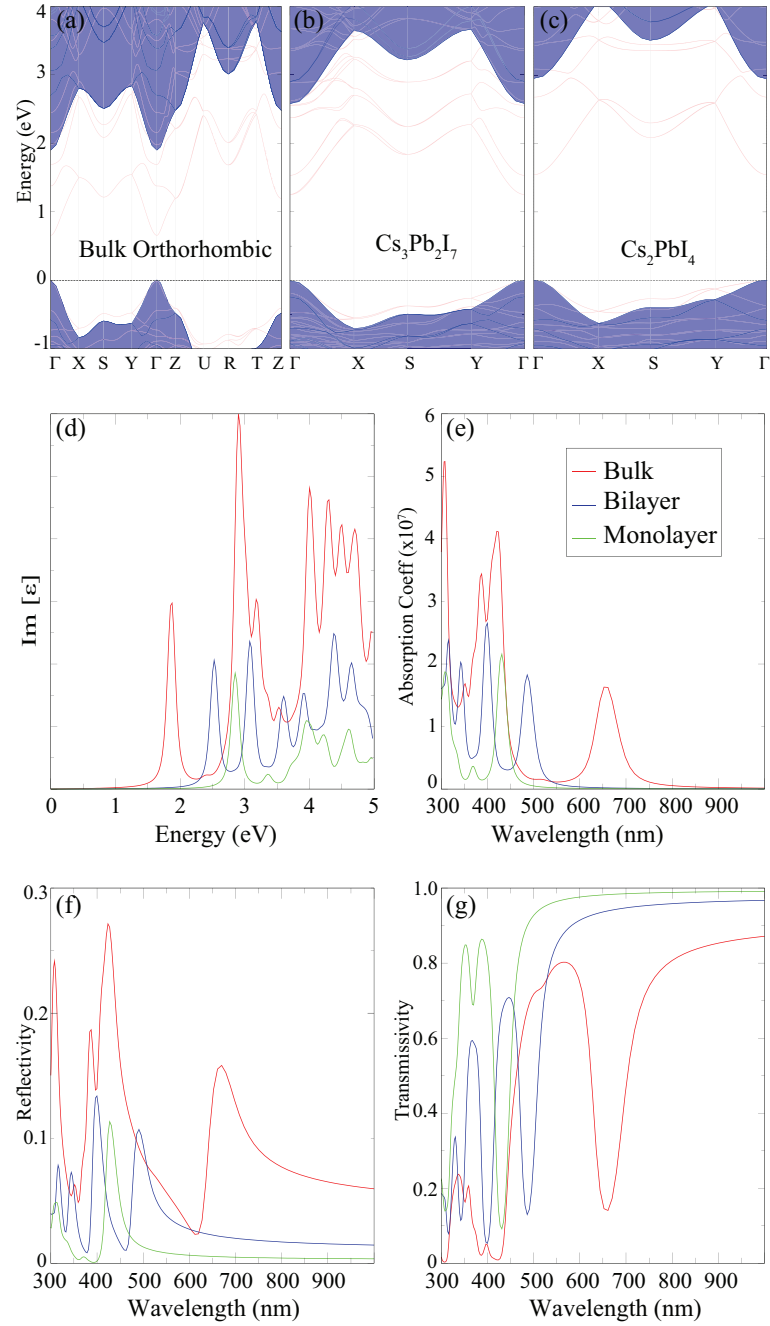


Figure 4.3. Electronic band dispersions of (a) bulk, (b) bilayer, (c) monolayer structures of orthorhombic CsPbI₃ crystal. The layer dependent optical properties of CsPbI₃. (a) Imaginary part of dielectric function, (b) absorption coefficient, (c) reflectivity, and (d) transmissivity of bulk, bilayer, and monolayer CsPbI₃.

sented in Fig. 4.3 (d-g) frequency dependent imaginary dielectric function, absorption coefficient, reflectivity and transmissivity of bulk, bilayer, and monolayer structures are calculated. The imaginary part of dielectric functions reveals that bulk, bilayer and monolayer CsPbI₃ display onset around 1.86, 2.53, and 2.85 eV, respectively. In addition, absorption spectrum shows that first prominent absorption peaks of bulk, bilayer and monolayer orthorhombic CsPbI₃ locate around 657, 486, and 431 nm, respectively, indicating a significant blue shift driven by dimensional reduction. As seen in Fig. 4.3 (f), the reflectivity increases gradually once the layer number increases, reaching a maximum of 30% for bulk. Regardless of the thickness of the material, the most significant peak of reflectivity around the visible range located in between 400-450 nm. Moreover, as illustrated in Fig. 4.3 (g), as the number of the layer increases the transmissivity of the material decreases. It is seen that while the transmissivity of monolayer and bilayer CsPbI₃ is very high in the 600-1000 nm, that of bulk and bilayer is almost zero near the 400 nm.

4.3. Enhanced Stability via Encapsulation

One of the most important issue of perovskite materials are their instability. To the best of our knowledge, the most stable solar cell based on the perovskite has a one-year of lifetime.(Grancini *et al.*, 2017) In addition, as a method to enhance the stability, encapsulation is reported earlier as providing both light and water resistance.(Raja *et al.*, 2016) In addition, it was reported that the encapsulation of CH₃NH₃PbI₃ perovskite by monolayer graphene dramatically enhance the stability of the material and maintain the optical properties upon exposure to moisture and high temperature.(Wang *et al.*, 2018) Regarding the possible encapsulating materials for the thinnest orthorhombic structure, recently synthesized SnS₂(Su *et al.*, 2014) has quite matching lattice parameters.

In order to examine the stability of the SnS₂-encapsulated monolayers we performed three different sets of molecular dynamic (MD) calculations. In order to construct the heterostructure, we put 1×2×1 supercell of monolayer CsPbI₃ in between two layers of 2×3×1 rectangular supercells of 1T SnS₂.

In the first set the temperature of the system is kept at 300 K for 5 ps with a time step of 1 fs. In the second and third sets the temperature is increased from 0 to 500 K up

to 2 ps and 5 ps with a time step of 1 fs, respectively. The side view geometric structures of all the three cases at the beginning and end of the MD simulations are shown in the Fig. 4.4. It is clear that, as the material is heated, the perovskite exhibits small distortions, while the SnS_2 layers remain quite robust. No geometric reconstructions or broken bonds occur in SnS_2 with increasing temperature. However, the Cs atoms of the perovskite are highly mobile. Fortunately, the SnS_2 layers interact strongly with perovskite and prevent the perovskite from breaking down up to 500K. Moreover, the SnS_2 layer not only prevents the material from being disassembled up with increasing temperature increases, but also protects the material against environmental factors such as moisture, oxidation and impurities.

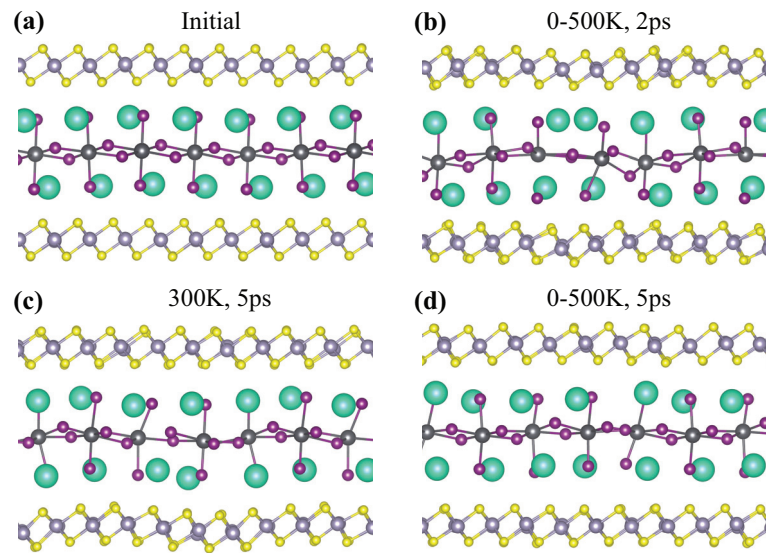


Figure 4.4. Molecular dynamics simulations of Cs_2PbI_4 monolayer (a) at 300 K for 5 ps, (b) from 0 to 500 K for 2 ps, (c) from 0 to 500 K for 5 ps.

CHAPTER 5

WATER-INDUCED DIMENSIONAL TRANSITION FROM CsPbBr₃ NANOWIRE TO BUNDLES

Recent progress in colloidal synthesis has given rise to a growing concentration on halide perovskites. Because of the highly ionic characteristics of perovskites, the matter of stability particularly arises when they are exposed to polar solvents like water. In this study, it is examined water-induced structural evolution of CsPbBr₃ by conducting state-of-the-art calculations of first principles and experiments. Although optic images show the slow degradation of the CsPbBr₃ yellowish structure in light of daytime, images under ultraviolet light indicate that crystals are degraded in two steps; the evolution from blue-emitting to green-emitting and then to full degrading phase. It is observed that the CsPbBr₃ NWs which are as-synthesized, exhibit blue emission under UV and first CsPbBr₃ NWs undergo a water-conducted structural evolution to form bundles. The formation of these bundles is also seen as showing long-term environmental stability.

Even if the intrinsic stability of the all-inorganic perovskites is better than the organometallic halides, instability is always a struggle, especially when exposed to moisture and polar solvents, e.g. acetone, ethanol, water, etc. (Kovalenko *et al.*, 2017; Iso and Isobe, 2018; Huang *et al.*, 2017; Li *et al.*, 2017) Yuan *et al.* found that CsPbI₃ quantum dots can be damaged by light and humidity. (Yuan *et al.*, 2017)

Recent researches on perovskite solar cells (PSCs) illustrates the material defect sensitivity and instability. (Huang *et al.*, 2017) Lejitas *et al.* reported strategies to address the problems of CsPbX₃ nanocrystals' structural, thermal and atmospheric degradation. (Leijtens *et al.*, 2017) Apart from experimental studies, enormous attempts were also made on PSCs by performing density functional density theory (DFT). (İyikanat *et al.*, 2017; Yin *et al.*, 2015; Geng *et al.*, 2014; Kawai *et al.*, 2015; Haruyama *et al.*, 2015) The CsPbBr₃ phase which is alternative to other perovskite phases, recently has exhibited the best optoelectronic properties of organic-inorganic hybrid lead halides perovskites. (Bekenstein *et al.*, 2015; Protesescu *et al.*, 2015)

CsPbBr₃ crystals were captured at various times under daylight as well as UV

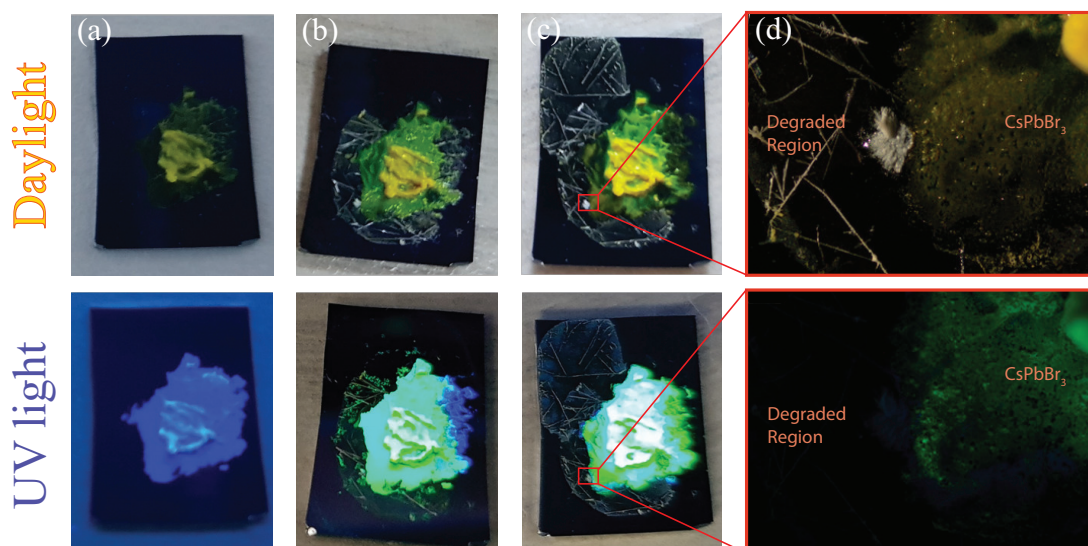


Figure 5.1. Images of CsPbBr₃; (a) at first after drop-casting, (b) 24 hours and (c) 144 hours after water treatment, respectively under daylight and UV light. The focused area in (d) shows an optic microscope images under daylight and UV light.

light (254 nm) and shown in Fig. 5.1 in both structural and electronic water interaction developments. Hexane solution is dropped on the substrate. Then the sample was found to be yellowish, greenish like color explicit blue under UV, under daylight. As seen in Fig. 5.1 (b), CsPbBr₃ becomes expressly green under UV light, but small blue emitting regions still exist. More water interactions results in developing of relatively large, white crystals which do not demonstrate any emission under UV light because of degradation (Fig. 5.1 (c) and (d)). According to monitoring the water induced crystal evolution and degradation results indicate that there is two steps such as evolution to a phase which emits green colour and complete degradation of CsPbBr₃ crystals.

5.1. Water-induced Evolution from Blue to Green Light Emitting Structure

While CsPbBr₃ maintains a yellowish color due to water interaction, it can be witnessed that the water induced evolution from blue emitting phase to green emitting

phase under ultraviolet light. As seen in Fig. 5.2 (a), emission characteristics demonstrate evolution from 450 nm single PL peak to a transition PL peak which consisting of two peaks. One of these peaks (peak at 450 nm) is assigned to individual NWs, the other

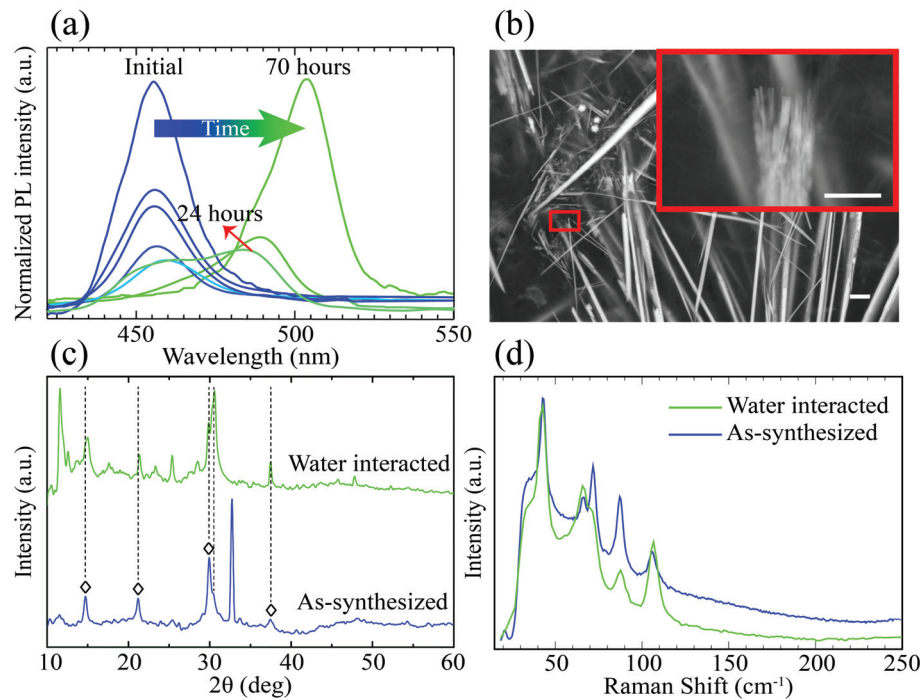


Figure 5.2. (a) Time-dependent photoluminescence of NWs interacting with water, (b) SEM image after 24 hours of interaction with the resulting NW structure, and (c)-(d) are both as-synthesized and water-interacted samples' XRD measurement and Raman spectra. Scale bars are $2 \mu\text{m}$.

one is assigned to bundles which are formed by water interacted nanowires in the first 24 hours. And nanowires originated PL peak reduces in time while the bundles originated one increases after 70 hours.

According to SEM image, the evolution of larger crystals (rods) which are in sizes of $>5 \mu\text{m}$ from single NWs is demonstrated in Fig. 5.2 (b). Moreover, the inset of Fig. 5.2 (b) also reveals that these rods are consisting of many nanowires. The formation of bundles is affirmed by these results. It is clear that the red-shift is originated from, nanowire to bundle evolution induced quantum confinement effect.

From Raman measurements and x-ray diffraction measurements, evolution of crystal structure of CsPbBr_3 perovskites is determined due to water interaction, as shown

in Fig. 5.2 (c) and (d). It is observed that the blue and green emitting phases have the identical crystal structure from x-ray diffractogram. Both cases show the same Xrd pattern as 15° , 22° , 30° , and 31° 2θ reflections. Moreover, formed least amount of Cs_4PbBr_6 is observed from extra 2θ reflections at 12° and 25° . (Zhang *et al.*, 2017) When the vibrational characteristics of the blue and green emitting structures are compared, unchanged perovskite crystal structure can be investigated, as seen in Fig. 5.2 (d).

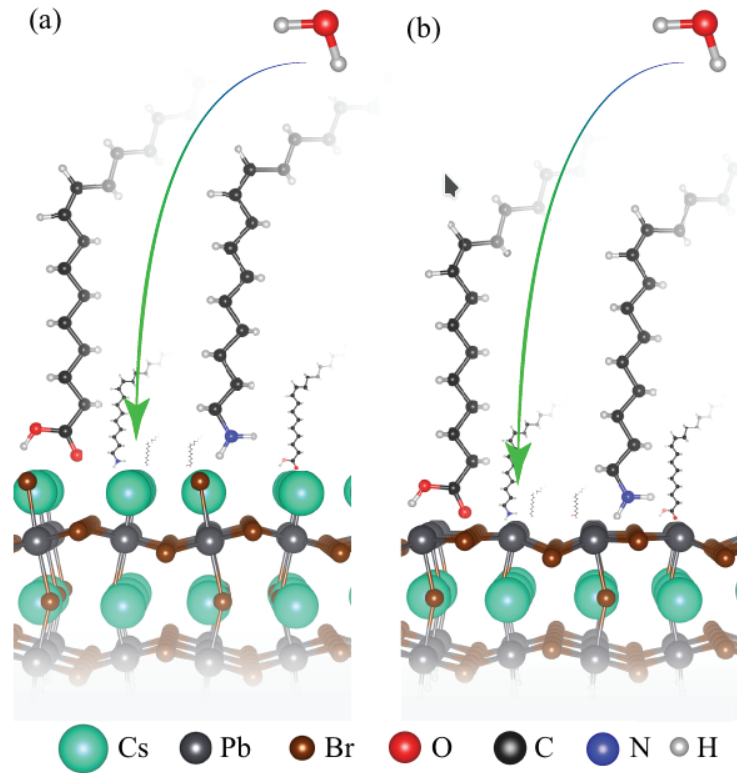


Figure 5.3. (a) Cs-terminated and (b) Pb-terminated surfaces of CsPbBr_3 .

DFT calculations are also used for better understanding of water-induced evolution from nanowire to bundle. The bulk form of orthorhombic CsPbBr_3 is cutted as Cs-terminated and Pb-terminated surfaces as investigated in Fig. 5.3 (a) and (b), respectively. In order to investigate the interaction between perovskite surfaces and water molecule (H_2O), binding energy (E_b) calculation results are compared. It is investigated that binding energies (E_b) of water molecule on Cs-terminated surface and on Pb-terminated surface are found 649 meV and 808 meV, respectively. Additionally, binding energies (E_b) of oleic acid (OA), oleylamine (OAm) on different surfaces are compared with water

molecule binding energies. For Cs-terminated surface, E_b of OA and OAm are calculated as 698 meV which is comparable with binding energy of H_2O , and 463 meV, respectively. On the other hand, for Pb-terminated surface, E_b of OA and OAm are investigated as 221 meV and 874 meV which is comparable with binding energy of H_2O on the same surface, respectively. To be able to completely discuss the ligands, water molecule and perovskite surface interactions, binding energies of H_2O with OAm and OA are found to be 550 meV and 898 meV, respectively. This results indicate that for OA it is more favorable to bind with H_2O molecule. Therefore, the presence of water molecule causes the detachment of OA ligand from the surfaces which results in evolution from nanowire to bundle. Last but not least, the absence of OA may leads to slight phase transition from $CsPbBr_3$ to Cs_4PbBr_6 .(Udayabhaskararao *et al.*, 2017)

CHAPTER 6

CONCLUSIONS

Modern life develops around the energy and technological advances and all new inventions increase the energy demand. The way we produce energy is one of the strong causes of climate change. That is why the best solution is renewable energy sources in order to overcome this issue for now and the future. The implementation of renewable energy can be a starting point for acting towards the heart of this issue. The key parameter for this revolution is that the solution needs to be seemed cost reduction. Especially for renewable energy, low-cost material research has high priority. Perovskites are promising materials in this regard. Perovskite materials have an ABX_3 general formula. A is organic such as $CH_3NH_3^+$ (MA), $HC(NH_2)_2^+$ (FA) or inorganic such as Cs^+ cation, B is metal cation as Pb^{2+} , Sn^{2+} , Sb^{2+} , and X is halide anion as Br^- , Cl^- , I^- in the crystal structure. The first type and second type are known as organic-inorganic perovskite and the all-inorganic perovskite, respectively. The discovery of $MAPbI_3$ as a photosensitizer in solar cell (DSSC's) in 2009 has led to more attention being paid to these materials. Among those, all-inorganic cesium lead halide perovskites (ILHPs) have attracted tremendous attention for recent years. Due to their extraordinary photovoltaic features, ILHPs are gaining wide variety of role as strong contenders in optoelectronic research with tunable band-gap, large absorption cross-section, long carrier lifetime, and high carrier mobility. The fabrication of ILHP nanostructures with controllable size and dimensionality have become very important. The photoluminescence characteristics of colloidal lead halide perovskite nanocrystals can be tuned by reducing their dimensionality. Therefore, in this thesis, experimentally tunable degree of quantum confinement of luminescent $CsPbBr_3$ nanoplatelets were achieved by means of a novel coating approach via electrospaying. Furthermore, DFT-based calculations were performed in order to investigate the thickness dependent properties of $CsPbI_3$ perovskite and water induced $CsPbBr_3$ NWs to bundles formation is investigated.

Firstly, one pot synthesis and coating of $CsPbBr_3$ nanoplatelets by electrospaying from precursor solution was investigated as facile and low cost process. Without using

anti-solvent or heating for crystallization, simply prepared precursor solution was sprayed under electric field onto the ITO. It was found that the proposed method leads to formation of CsPbBr₃ nanoplatelets. By increasing the OAm fraction in precursor solution, the degree of quantum confinement of nanoplatelets goes up as OAm acts as intercalation agent between nanoplatelets. In addition, the great potential of electrospraying method for various applications was introduced by millimeter sized patterning.

Secondly, thickness dependency of characteristic properties of the orthorhombic phase of CsPbI₃ perovskite was investigated via state-of-the-art first-principles calculations. Total energy and phonon calculations revealed that only bilayers and monolayers with Cs-I terminated surfaces may form stable thin structures. It was showed that energy bandgap significantly increases, as the thickness of the perovskite decreases from bulk to bilayer and then monolayer due to size effect. Moreover, the calculations on the optical response of the structures (dielectric function, absorption coefficient, reflectivity, and transmissivity) showed that reduction in thickness also leads to the blue shift of the absorption edge of the optical spectra.

Thirdly, water induced transformation from CsPbBr₃ nanowires to bundles were investigated via experimental results and state-of-the-art computational techniques.(Akbalı *et al.*, 2018) It was observed that water molecule interacts with surfactants (oleylamine, oleic acid) and causes the detachment of them from surface of perovskite NWs. Without surfactants, NWs tend to get together and form bundles. This transformation leads to a red shift in PL spectrum from blue region to green region due to losing of quantum confinement.

To summarize, experimental and theoretical studies on dimension dependent optoelectronic properties of cesium lead halide have been presented in this thesis. Control of dimensionality helps understanding connections between size and optic, electronic properties of the perovskite crystals from a fundamental point of view. Thickness tunable CsPbBr₃ nanoplatelets, transformation from NWs to bundles with study of their optical properties experimentally were achieved. Furthermore, thickness dependent optic and electronic properties of CsPbI₃ perovskites were obtained via state-of-the-art first-principles calculations. We believe that the results of this thesis successfully will enlighten the characteristic properties of low-dimensional perovskites for optoelectronic applications.

REFERENCES

- Aierken, Y., H. Sahin, F. İyikanat, S. Horzum, A. Suslu, B. Chen, R. T. Senger, S. Tongay, and F. M. Peeters (2015). Portlandite crystal: Bulk, bilayer, and monolayer structures. *Physical Review B* 91(24), 245413.
- Akbali, B., G. Topcu, T. Guner, M. Ozcan, M. M. Demir, and H. Sahin (2018). CsPbBr₃ perovskites: Theoretical and experimental investigation on water-assisted transition from nanowire formation to degradation. *Physical Review Materials* 2(3), 034601.
- Akkerman, Q. A., V. D'Innocenzo, S. Accornero, A. Scarpellini, A. Petrozza, M. Prato, and L. Manna (2015). Tuning the optical properties of cesium lead halide perovskite nanocrystals by anion exchange reactions. *Journal of the American Chemical Society* 137(32), 10276–10281.
- Amgar, D., A. Stern, D. Rotem, D. Porath, and L. Etgar (2017). Tunable length and optical properties of CsPbX₃ (X = Cl, Br, I) nanowires with a few unit cells. *Nano letters* 17(2), 1007–1013.
- Ban, M., Y. Zou, J. P. Rivett, Y. Yang, T. H. Thomas, Y. Tan, T. Song, X. Gao, D. Credington, F. Deschler, *et al.* (2018). Solution-processed perovskite light emitting diodes with efficiency exceeding 15% through additive-controlled nanostructure tailoring. *Nature communications* 9(1), 3892.
- Bekenstein, Y., B. A. Koscher, S. W. Eaton, P. Yang, and A. P. Alivisatos (2015). Highly luminescent colloidal nanoplates of perovskite cesium lead halide and their oriented assemblies. *Journal of the American Chemical Society* 137(51), 16008–16011.
- Blöchl, P. (1994). Generalized gradient approximation made simple. *Phys. Rev. B* 50, 17953–17979.
- Brandt, R. E., V. Stevanović, D. S. Ginley, and T. Buonassisi (2015). Identifying defect tolerant semiconductors with high minority-carrier lifetimes: beyond hybrid lead

halide perovskites. *Mrs Communications* 5(2), 265–275.

Ceperley, D. M. and B. Alder (1980). Ground state of the electron gas by a stochastic method. *Physical Review Letters* 45(7), 566.

Chen, Q., H. Zhou, T.-B. Song, S. Luo, Z. Hong, H.-S. Duan, L. Dou, Y. Liu, and Y. Yang (2014). Controllable self-induced passivation of hybrid lead iodide perovskites toward high performance solar cells. *Nano letters* 14(7), 4158–4163.

Cho, H., S.-H. Jeong, M.-H. Park, Y.-H. Kim, C. Wolf, C.-L. Lee, J. H. Heo, A. Sadhanala, N. Myoung, S. Yoo, *et al.* (2015). Overcoming the electroluminescence efficiency limitations of perovskite light-emitting diodes. *Science* 350(6265), 1222–1225.

Cho, H., C. Wolf, J. S. Kim, H. J. Yun, J. S. Bae, H. Kim, J.-M. Heo, S. Ahn, and T.-W. Lee (2017). High-efficiency solution-processed inorganic metal halide perovskite light-emitting diodes. *Advanced Materials* 29(31), 1700579.

Dastidar, S., C. J. Hawley, A. D. Dillon, A. D. Gutierrez-Perez, J. E. Spanier, and A. T. Fafarman (2017). Quantitative phase-change thermodynamics and metastability of perovskite-phase cesium lead iodide. *The journal of physical chemistry letters* 8(6), 1278–1282.

Dou, L., A. B. Wong, Y. Yu, M. Lai, N. Kornienko, S. W. Eaton, A. Fu, C. G. Bischak, J. Ma, T. Ding, *et al.* (2015). Atomically thin two-dimensional organic-inorganic hybrid perovskites. *Science* 349(6255), 1518–1521.

Eperon, G. E., G. M. Paterno, R. J. Sutton, A. Zampetti, A. A. Haghighirad, F. Cacialli, and H. J. Snaith (2015). Inorganic caesium lead iodide perovskite solar cells. *Journal of Materials Chemistry A* 3(39), 19688–19695.

Gamliel, S., A. Dymshits, S. Aharon, E. Terkieltaub, and L. Etgar (2015). Micrometer sized perovskite crystals in planar hole conductor free solar cells. *The Journal of Physical Chemistry C* 119(34), 19722–19728.

- Geng, W., L. Zhang, Y.-N. Zhang, W.-M. Lau, and L.-M. Liu (2014). First-principles study of lead iodide perovskite tetragonal and orthorhombic phases for photovoltaics. *The Journal of Physical Chemistry C* 118(34), 19565–19571.
- Grancini, G., C. Roldán-Carmona, I. Zimmermann, E. Mosconi, X. Lee, D. Martineau, S. Narbey, F. Oswald, F. De Angelis, M. Graetzel, *et al.* (2017). One-year stable perovskite solar cells by 2d/3d interface engineering. *Nature communications* 8, 15684.
- Han, W.-Q., L. Wu, Y. Zhu, K. Watanabe, and T. Taniguchi (2008). Structure of chemically derived mono- and few-atomic-layer boron nitride sheets. *Applied Physics Letters* 93(22), 223103.
- Haruyama, J., K. Sodeyama, L. Han, and Y. Tateyama (2015). First-principles study of ion diffusion in perovskite solar cell sensitizers. *Journal of the American Chemical Society* 137(32), 10048–10051.
- Hassan, Y., Y. Song, R. D. Pensack, A. I. Abdelrahman, Y. Kobayashi, M. A. Winnik, and G. D. Scholes (2016). Structure-tuned lead halide perovskite nanocrystals. *Advanced materials* 28(3), 566–573.
- Henkelman, G., A. Arnaldsson, and H. Jónsson (2006). A fast and robust algorithm for bader decomposition of charge density. *Computational Materials Science* 36(3), 354–360.
- Hong, S. C., G. Lee, K. Ha, J. Yoon, N. Ahn, W. Cho, M. Park, and M. Choi (2017). Precise morphology control and continuous fabrication of perovskite solar cells using droplet-controllable electro-spray coating system. *ACS applied materials & interfaces* 9(9), 7879–7884.
- Hong, X., T. Ishihara, and A. Nurmikko (1992a). Dielectric confinement effect on excitons in pbi 4-based layered semiconductors. *Physical Review B* 45(12), 6961.
- Hong, X., T. Ishihara, and A. Nurmikko (1992b). Photoconductivity and electroluminescence in lead iodide based natural quantum well structures. *Solid state communica-*

tions 84(6), 657–661.

Huang, H., M. I. Bodnarchuk, S. V. Kershaw, M. V. Kovalenko, and A. L. Rogach (2017). Lead halide perovskite nanocrystals in the research spotlight: stability and defect tolerance. *ACS energy letters* 2(9), 2071–2083.

Iso, Y. and T. Isobe (2018). Synthesis, luminescent properties, and stabilities of cesium lead halide perovskite nanocrystals. *ECS Journal of Solid State Science and Technology* 7(1), R3040–R3045.

İyikanat, F., E. Sari, and H. Sahin (2017). Thinning cspb 2 br 5 perovskite down to monolayers: Cs-dependent stability. *Physical Review B* 96(15), 155442.

Kagan, C., D. Mitzi, and C. Dimitrakopoulos (1999). Organic-inorganic hybrid materials as semiconducting channels in thin-film field-effect transistors. *Science* 286(5441), 945–947.

Kang, J. and L.-W. Wang (2017). High defect tolerance in lead halide perovskite cspbbr3. *The journal of physical chemistry letters* 8(2), 489–493.

Kawai, H., G. Giorgi, A. Marini, and K. Yamashita (2015). The mechanism of slow hot-hole cooling in lead-iodide perovskite: first-principles calculation on carrier lifetime from electron–phonon interaction. *Nano letters* 15(5), 3103–3108.

Kim, Y.-H., H. Cho, and T.-W. Lee (2016). Metal halide perovskite light emitters. *Proceedings of the National Academy of Sciences* 113(42), 11694–11702.

Kohn, W. and L. J. Sham (1965). Self-consistent equations including exchange and correlation effects. *Physical review* 140(4A), A1133.

Kojima, A., K. Teshima, Y. Shirai, and T. Miyasaka (2009). Organometal halide perovskites as visible-light sensitizers for photovoltaic cells. *Journal of the American Chemical Society* 131(17), 6050–6051.

- Kovalenko, M. V., L. Protesescu, and M. I. Bodnarchuk (2017). Properties and potential optoelectronic applications of lead halide perovskite nanocrystals. *Science* 358(6364), 745–750.
- Kresse, G. and J. Hafner (1993). Ab initio molecular dynamics for liquid metals. *Physical Review B* 47(1), 558.
- Kresse, G. and J. Hafner (1996). 14251); g. kresse, j. furthmüller. *Phys. Rev. B* 54, 11169.
- Kresse, G. and D. Joubert (1999). From ultrasoft pseudopotentials to the projector augmented-wave method. *Physical Review B* 59(3), 1758.
- Kulbak, M., D. Cahen, and G. Hodes (2015). How important is the organic part of lead halide perovskite photovoltaic cells? efficient cspbbr3 cells. *The journal of physical chemistry letters* 6(13), 2452–2456.
- Kumar, P. S., J. Sundaramurthy, S. Sundarrajan, V. J. Babu, G. Singh, S. I. Allakhverdiev, and S. Ramakrishna (2014). Hierarchical electrospun nanofibers for energy harvesting, production and environmental remediation. *Energy & environmental science* 7(10), 3192–3222.
- Leijtens, T., K. Bush, R. Cheacharoen, R. Beal, A. Bowring, and M. D. McGehee (2017). Towards enabling stable lead halide perovskite solar cells; interplay between structural, environmental, and thermal stability. *Journal of Materials Chemistry A* 5(23), 11483–11500.
- Li, X., F. Cao, D. Yu, J. Chen, Z. Sun, Y. Shen, Y. Zhu, L. Wang, Y. Wei, Y. Wu, *et al.* (2017). All inorganic halide perovskites nanosystem: synthesis, structural features, optical properties and optoelectronic applications. *Small* 13(9), 1603996.
- Li, X., Y. Wu, S. Zhang, B. Cai, Y. Gu, J. Song, and H. Zeng (2016). Cspx3 quantum dots for lighting and displays: room-temperature synthesis, photoluminescence superiorities, underlying origins and white light-emitting diodes. *Advanced Functional Materials* 26(15), 2435–2445.

- Liang, K., D. B. Mitzi, and M. T. Prikas (1998). Synthesis and characterization of organic-inorganic perovskite thin films prepared using a versatile two-step dipping technique. *Chemistry of materials* 10(1), 403–411.
- Mak, K. F., C. Lee, J. Hone, J. Shan, and T. F. Heinz (2010). Atomically thin mos 2: a new direct-gap semiconductor. *Physical review letters* 105(13), 136805.
- Makarov, N. S., S. Guo, O. Isaienko, W. Liu, I. Robel, and V. I. Klimov (2016). Spectral and dynamical properties of single excitons, biexcitons, and trions in cesium–lead-halide perovskite quantum dots. *Nano letters* 16(4), 2349–2362.
- Marronnier, A., G. Roma, S. Boyer-Richard, L. Pedesseau, J.-M. Jancu, Y. Bonnassieux, C. Katan, C. C. Stoumpos, M. G. Kanatzidis, and J. Even (2018). Anharmonicity and disorder in the black phases of cesium lead iodide used for stable inorganic perovskite solar cells. *ACS nano* 12(4), 3477–3486.
- Mitzi, D. B., C. Feild, Z. Schlesinger, and R. Laibowitz (1995). Transport, optical, and magnetic properties of the conducting halide perovskite $\text{CH}_3\text{NH}_3\text{SnI}_3$. *Journal of Solid State Chemistry* 114(1), 159–163.
- Molina-Sánchez, A. (2018). Excitonic states in semiconducting two-dimensional perovskites. *ACS Applied Energy Materials* 1(11), 6361–6367.
- Naphade, R., S. Nagane, G. S. Shanker, R. Fernandes, D. Kothari, Y. Zhou, N. P. Padture, and S. Ogale (2015). Hybrid perovskite quantum nanostructures synthesized by electrospray antisolvent–solvent extraction and intercalation. *ACS applied materials & interfaces* 8(1), 854–861.
- Nasilowski, M., B. Mahler, E. Lhuillier, S. Ithurria, and B. Dubertret (2016). Two-dimensional colloidal nanocrystals. *Chemical Reviews* 116(18), 10934–10982.
- Neto, A. C. and K. Novoselov (2011). New directions in science and technology: two-dimensional crystals. *Reports on Progress in Physics* 74(8), 082501.

Novoselov, K. S., A. K. Geim, S. V. Morozov, D. Jiang, Y. Zhang, S. V. Dubonos, I. V. Grigorieva, and A. A. Firsov (2004). Electric field effect in atomically thin carbon films. *science* 306(5696), 666–669.

Pan, J., L. N. Quan, Y. Zhao, W. Peng, B. Murali, S. P. Sarmah, M. Yuan, L. Sinatra, N. M. Alyami, J. Liu, *et al.* (2016). Highly efficient perovskite-quantum-dot light-emitting diodes by surface engineering. *Advanced Materials* 28(39), 8718–8725.

Perdew, J. P. and A. Zunger (1981). Self-consistent equations including exchange and correlation effects *phys. Rev. B* 23, 5048–79.

Protesescu, L., S. Yakunin, M. I. Bodnarchuk, F. Krieg, R. Caputo, C. H. Hendon, R. X. Yang, A. Walsh, and M. V. Kovalenko (2015). Nanocrystals of cesium lead halide perovskites (cspbx₃, x= cl, br, and i): novel optoelectronic materials showing bright emission with wide color gamut. *Nano letters* 15(6), 3692–3696.

Radisavljevic, B., A. Radenovic, J. Brivio, i. V. Giacometti, and A. Kis (2011). Single-layer mos₂ transistors. *Nature nanotechnology* 6(3), 147.

Raja, S. N., Y. Bekenstein, M. A. Koc, S. Fischer, D. Zhang, L. Lin, R. O. Ritchie, P. Yang, and A. P. Alivisatos (2016). Encapsulation of perovskite nanocrystals into macroscale polymer matrices: enhanced stability and polarization. *ACS applied materials & interfaces* 8(51), 35523–35533.

Ramesh, M., K. M. Boopathi, T.-Y. Huang, Y.-C. Huang, C.-S. Tsao, and C.-W. Chu (2015). Using an airbrush pen for layer-by-layer growth of continuous perovskite thin films for hybrid solar cells. *ACS applied materials & interfaces* 7(4), 2359–2366.

Rose, G. (1839). Beschreibung einiger neuen mineralien des ural. *Annalen der Physik* 124(12), 551–573.

Schmidt, L. C., A. Pertegás, S. González-Carrero, O. Malinkiewicz, S. Agouram, G. Miñguez Espallargas, H. J. Bolink, R. E. Galian, and J. Peñrez-Prieto (2014). Non-template synthesis of ch₃nh₃pbb₃ perovskite nanoparticles. *Journal of the American*

Chemical Society 136(3), 850–853.

Shamsi, J., Z. Dang, P. Bianchini, C. Canale, F. Di Stasio, R. Brescia, M. Prato, and L. Manna (2016). Colloidal synthesis of quantum confined single crystal cspbbr₃ nanosheets with lateral size control up to the micrometer range. *Journal of the American Chemical Society* 138(23), 7240–7243.

Sichert, J. A., Y. Tong, N. Mutz, M. Vollmer, S. Fischer, K. Z. Milowska, R. García Cortadella, B. Nickel, C. Cardenas-Daw, J. K. Stolarczyk, *et al.* (2015). Quantum size effect in organometal halide perovskite nanoplatelets. *Nano letters* 15(10), 6521–6527.

Splendiani, A., L. Sun, Y. Zhang, T. Li, J. Kim, C.-Y. Chim, G. Galli, and F. Wang (2010). Emerging photoluminescence in monolayer mos₂. *Nano letters* 10(4), 1271–1275.

Stranks, S. D., G. E. Eperon, G. Grancini, C. Menelaou, M. J. Alcocer, T. Leijtens, L. M.

Herz, A. Petrozza, and H. J. Snaith (2013). Electron-hole diffusion lengths exceeding 1 micrometer in an organometal trihalide perovskite absorber. *Science* 342(6156), 341–344.

Su, G., V. G. Hadjiev, P. E. Loya, J. Zhang, S. Lei, S. Maharjan, P. Dong, P. M. Ajayan, J. Lou, and H. Peng (2014). Chemical vapor deposition of thin crystals of layered semiconductor sns₂ for fast photodetection application. *Nano letters* 15(1), 506–513.

Sutton, R. J., G. E. Eperon, L. Miranda, E. S. Parrott, B. A. Kamino, J. B. Patel, M. T. Hörantner, M. B. Johnston, A. A. Haghighirad, D. T. Moore, *et al.* (2016). Bandgap-tunable cesium lead halide perovskites with high thermal stability for efficient solar cells. *Advanced Energy Materials* 6(8), 1502458.

Sutton, R. J., M. R. Filip, A. A. Haghighirad, N. Sakai, B. Wenger, F. Giustino, and H. J. Snaith (2018). Cubic or orthorhombic? revealing the crystal structure of metastable black-phase cspbi₃ by theory and experiment. *ACS Energy Letters* 3(8), 1787–1794.

Togo, A., F. Oba, and I. Tanaka (2008). First-principles calculations of the ferroelastic transition between rutile-type and cacl₂-type sio₂ at high pressures. *Physical Review*

B 78(13), 134106.

Tong, Y., E. Bladt, M. F. Aygüler, A. Manzi, K. Z. Milowska, V. A. Hintermayr, P. Docompo, S. Bals, A. S. Urban, L. Polavarapu, *et al.* (2016). Highly luminescent cesium lead halide perovskite nanocrystals with tunable composition and thickness by ultrasonication. *Angewandte Chemie International Edition* 55(44), 13887–13892.

Tyagi, P., S. M. Arveson, and W. A. Tisdale (2015). Colloidal organohalide perovskite nanoplatelets exhibiting quantum confinement. *The journal of physical chemistry letters* 6(10), 1911–1916.

Udayabhaskararao, T., L. Houben, H. Cohen, M. Menahem, I. Pinkas, L. Avram, T. Wolf, A. Teitelboim, M. Leskes, O. Yaffe, *et al.* (2017). A mechanistic study of phase transformation in perovskite nanocrystals driven by ligand passivation. *Chemistry of Materials* 30(1), 84–93.

Wang, Q. H., K. Kalantar-Zadeh, A. Kis, J. N. Coleman, and M. S. Strano (2012). Electronics and optoelectronics of two-dimensional transition metal dichalcogenides. *Nature nanotechnology* 7(11), 699.

Wang, Z., Q. Ou, Y. Zhang, Q. Zhang, H. Y. Hoh, and Q. Bao (2018). Degradation of two-dimensional $\text{CH}_3\text{NH}_3\text{PbI}_3$ perovskite and $\text{CH}_3\text{NH}_3\text{PbI}_3/\text{graphene}$ heterostructure. *ACS applied materials & interfaces* 10(28), 24258–24265.

Wei, Z., A. Perumal, R. Su, S. Sushant, J. Xing, Q. Zhang, S. T. Tan, H. V. Demir, and Q. Xiong (2016). Solution-processed highly bright and durable cesium lead halide perovskite light-emitting diodes. *Nanoscale* 8(42), 18021–18026.

Weidman, M. C., M. Seitz, S. D. Stranks, and W. A. Tisdale (2016). Highly tunable colloidal perovskite nanoplatelets through variable cation, metal, and halide composition. *ACS nano* 10(8), 7830–7839.

Wu, C., Y. Zou, T. Wu, M. Ban, V. Pecunia, Y. Han, Q. Liu, T. Song, S. Duhm, and B. Sun (2017). Improved performance and stability of all-inorganic perovskite

light-emitting diodes by antisolvent vapor treatment. *Advanced Functional Materials* 27(28), 1700338.

Yang, X., X. Zhang, J. Deng, Z. Chu, Q. Jiang, J. Meng, P. Wang, L. Zhang, Z. Yin, and J. You (2018). Efficient green light-emitting diodes based on quasi-two-dimensional composition and phase engineered perovskite with surface passivation. *Nature communications* 9(1), 570.

Yin, W.-J., J.-H. Yang, J. Kang, Y. Yan, and S.-H. Wei (2015). Halide perovskite materials for solar cells: a theoretical review. *Journal of Materials Chemistry A* 3(17), 8926–8942.

Yuan, G., C. Ritchie, M. Ritter, S. Murphy, D. E. Gómez, and P. Mulvaney (2017). The degradation and blinking of single CsPbI_3 perovskite quantum dots. *The Journal of Physical Chemistry C* 122(25), 13407–13415.

Yuan, S., Z.-K. Wang, M.-P. Zhuo, Q.-S. Tian, Y. Jin, and L.-S. Liao (2018). Self-assembled high quality CsPbBr_3 quantum dot films toward highly efficient light-emitting diodes. *ACS nano* 12(9), 9541–9548.

Yuan, Z., Y. Shu, Y. Xin, and B. Ma (2016). Highly luminescent nanoscale quasi-2d layered lead bromide perovskites with tunable emissions. *Chemical Communications* 52(20), 3887–3890.

Zhang, F., H. Zhong, C. Chen, X.-g. Wu, X. Hu, H. Huang, J. Han, B. Zou, and Y. Dong (2015). Brightly luminescent and color-tunable colloidal $\text{CH}_3\text{NH}_3\text{PbX}_3$ ($x = \text{Br, I, Cl}$) quantum dots: potential alternatives for display technology. *ACS nano* 9(4), 4533–4542.

Zhang, L., X. Yang, Q. Jiang, P. Wang, Z. Yin, X. Zhang, H. Tan, Y. M. Yang, M. Wei, B. R. Sutherland, *et al.* (2017). Ultra-bright and highly efficient inorganic based perovskite light-emitting diodes. *Nature communications* 8, 15640.

Zhang, Y., M. I. Saidaminov, I. Dursun, H. Yang, B. Murali, E. Alarousu, E. Yengel, B. A.

Alshankiti, O. M. Bakr, and O. F. Mohammed (2017). Zero-dimensional Cs_4PbBr_6 perovskite nanocrystals. *The journal of physical chemistry letters* 8(5), 961–965.